

# Politecnico di Torino

Department of Electronics and Telecommunications

Master in Biomedical Engineering



Master Degree Thesis

## Microwave imaging algorithms for biomedical applications

Supervisor

Prof. Francesca Vipiana

Dr. Jorge A. Tobon Vasquez

Candidate

Valeria Mariano

October 2019



# Abstract

MicroWave Imaging (MWI) technique has the goal to analyse and reconstruct the inside of an opaque body, exploiting the dielectric properties contrast between different materials. In this thesis, MWI technique is used to monitor the evolution in the human head after the stroke onset.

Currently, the most common adopted techniques are X-ray Computerized Tomography (CT) and magnetic resonance imaging (MRI). These two techniques are time-consuming and not portable, hence not suitable for a bedridden patient. Moreover, they are unapt for a continuous monitoring because X-ray technique has ionizing radiation and MRI is very expensive.

MWI can be an interesting option, indeed it has small size, low cost, non-ionizing radiations and low intensity; all these characteristics are necessary in a real-time monitoring device for a bedridden patient. MWI exploits algorithms for image reconstruction that solves inverse problems. The algorithms are divided into two classes: linear inversion methods and non-linear (iterative) methods. In this thesis two non-linear iterative algorithms are implemented and compared: the Distorted Born Iterative Method (DBIM) and the Contrast Source method (CS).

In the DBIM, Maxwell's equations are discretized in time and space with Finite Difference Time Domain method (FDTD). In this algorithm Two-step Iterative Shrinkage/Thresholding method (TwIST) is used to solve the linear equations set. It computes the current iteration using the two previous ones, so it has a higher convergence speed and it is more accurate than the one step iterative methods.

Instead, the CS inversion method searches electrical properties minimizing a cost functional. It uses a Finite Element Method (FEM) discretization with an unstructured, non-uniform and conformal mesh that allows to improve the reconstruction and to have boundaries of any type and shape.

In the thesis the comparison between the two imaging algorithms is organized as follows.

The first step of comparison is validation, i.e. input models are created with the same mechanism of the image reconstruction for each algorithm. This step is the furthest from

reality, but it is useful to understand if the algorithms work well with the easiest scenario.

The second step is the comparison of algorithms when input data are obtained with simulations. The simulations are realized with a tool of pre and post processor for numerical simulations and with an in-house FEM. Simulation is an intermediate step between the ideal and real case.

For these first steps, two models are used: in the first model there is a blood target in the coupling medium and surrounded by twelve antennas; in the second model there is a brain phantom with a blood target surrounded by twelve antennas and immersed in the coupling medium.

The last step of comparison is the analysis of algorithms behavior when inputs are measurements data. There is a description of laboratory instrumentation, device, phantom and also a characterization of measurements processing. In this part, the models used are three and all have a blood target in a brain phantom, immersed in the coupling medium and surrounded by twelve antennas. The difference between models is dimension and position of blood targets.

In the last part, there is a detailed analysis about the obtained results and possible future developments for both the algorithms.

# Abstract

La tecnica di imaging che utilizza le microonde (MWI) ha l'obiettivo di ricostruire l'interno di un corpo opaco, sfruttando il contrasto delle proprietà dielettriche nei diversi materiali. In questa tesi, la tecnica MWI è usata per monitorare l'evoluzione dello stato del paziente, in seguito all'insorgenza di un ictus.

Fino a oggi, le tecniche più utilizzate a tale scopo sono i Raggi X a Tomografia Computerizzata (TC) e la risonanza magnetica (MRI). Queste tecniche richiedono del tempo e non sono portabili, quindi non sono appropriate per un paziente allettato. Inoltre, la tecnica dei Raggi X sfrutta radiazioni ionizzanti e la Risonanza Magnetica è molto costosa, quindi risultano inadatte per un monitoraggio continuativo.

La tecnica MWI può essere un'alternativa interessante alle tecniche già esistenti, infatti il dispositivo ha piccole dimensioni, bassi costi, radiazioni non ionizzanti e a bassa intensità; tutte queste caratteristiche sono necessarie in un dispositivo di monitoraggio in tempo reale per un paziente allettato. Essa sfrutta algoritmi di ricostruzione dell'immagine che risolvono problemi inversi. Gli algoritmi sono suddivisi in due classi: metodi di inversione lineare e metodi non lineari iterativi. In questa tesi, due algoritmi non lineari iterativi sono implementati e comparati: il Distorted Born Iterative Method (DBIM) e il Contrast Source (CS).

Nel DBIM, le equazioni di Maxwell sono discretizzate nel tempo e nello spazio con il metodo Finite Difference Time Domain (FDTD). In questo algoritmo, il Two-step Iterative Shrinkage/Thresholding (TwIST) è usato per risolvere il sistema di equazioni lineari. Questo metodo calcola l'iterazione corrente usando le due precedenti, in questo modo raggiunge una convergenza più veloce e una ricostruzione più accurata rispetto ai metodi iterativi a singolo step.

Invece, l'algoritmo CS costruisce la distribuzione delle proprietà elettriche minimizzando un funzionale di costo. Esso effettua una discretizzazione basata sul Metodo agli Elementi Finiti (FEM) e utilizza una mesh non strutturata, non uniforme e conforme che permette di migliorare la ricostruzione e di avere dei contorni di qualsiasi tipo e forma.

Il confronto tra i due algoritmi di imaging è organizzato come segue.

Il primo passo è la validazione: i modelli in ingresso sono creati con lo stesso meccanismo di ricostruzione dell'immagine di ognuno dei due algoritmi. Questo step è il più lontano dalla realtà, ma è utile per capire se gli algoritmi lavorano bene con lo scenario più semplice.

Il secondo passo è il confronto delle performance degli algoritmi quando i dati di input sono ottenuti con delle simulazioni. Queste ultime sono state realizzate con un programma di elaborazione per simulazioni numeriche e con un in-house FEM. La simulazione è un passaggio intermedio tra il caso ideale e il caso reale.

Per questi primi due step, sono stati utilizzati due modelli: il primo è costituito da un target di sangue immerso nel mezzo di accoppiamento e circondato da dodici antenne; il secondo è costituito da un fantoccio che rappresenta il cervello con all'interno un target di sangue, essi sono immersi nel mezzo di accoppiamento e sono circondati da dodici antenne.

L'ultimo passo del confronto è l'analisi del comportamento degli algoritmi quando i dati in ingresso sono ottenuti attraverso delle misure in laboratorio.

È riportata una descrizione della strumentazione presente in laboratorio, del dispositivo, del fantoccio e una caratterizzazione del processo di elaborazione effettuato sui dati misurati. In questa sezione, i modelli usati sono tre e in tutti è presente un fantoccio che rappresenta il cervello (con all'interno un target di sangue), immerso nel mezzo di accoppiamento e circondato da dodici antenne. La differenza tra i modelli è nella dimensione e nella posizione del target di sangue.

Nell'ultima parte, è riportata un'analisi dettagliata sui risultati ottenuti e i possibili sviluppi futuri per entrambi gli algoritmi.

# Acknowledgements

I wish to thank all the people who have been close to me during my university years and my thesis period.

First of all, I owe my deepest gratitude to Prof. Francesca Vipiana, for the continuous support, for the indispensable advises and for the time dedicated to me. Her passion and admirable dedication to work are for me an inspiration.

I would like to thank Dr. Jorge Tobon for his constant help and for all the constructive discussions. I thank both of them for the hospitality and the trust.

I thank Prof. Panagiotis Kosmas and Dr. Olympia Karadima for providing me their algorithm and for the precious advises.

During my university years, I have known a lot of people that allowed me to become the person who I am. I begin from the first person that I met and also one of the most important: my ex roommate and best friend Andreina. Thank you because you made me feel at home and because you were my second family.

I thank also my colleagues and friends Marina and Valerio, with whom I shared these five years, the breaks between lessons, all the anxieties, and satisfactions.

During the thesis period, I was lucky to meet two girls, Gorana and Chiara. We helped each other in bad moments and we enjoyed the achievements together. Thank you for have shared with me this experience.

I would like to thank my boyfriend Franco for his advises in the most difficult moments, for the patience with which he waited for me when I was too busy with the study, because he gave me strength even with his presence and because he was close to me in moments when only he could have made the difference.

The last, but not least, I thank my family because they let me go even if the lack was the strongest presence in these years, for believing in me, for having followed each step and every little conquest. I dedicate this work to them and my boyfriend.

# Contents

<b>ABSTRACT [EN]</b> .....	III
<b>ABSTRACT [ITA]</b> .....	V
<b>ACKNOWLEDGEMENTS</b> .....	VII
<b>CONTENTS</b> .....	VIII
<b>LIST OF FIGURES</b> .....	XI
<b>LIST OF TABLES</b> .....	XV
<b>GLOSSARY</b> .....	XVI
<b>1. INTRODUCTION</b> .....	1
<b>1.1 STROKE AND IMAGING METHODS</b> .....	1
1.1.1 Ischemic stroke.....	1
1.1.2 Hemorrhagic stroke .....	2
<b>1.2 TECHNIQUES FOR STROKE IMAGING</b> .....	3
X-Rays.....	3
Magnetic Resonance Imaging (MRI) .....	4
<b>1.3 INNOVATIVE TECHNIQUE FOR STROKE IMAGING: MICROWAVE         IMAGING (MWI)</b> .....	4
1.3.1 Principles of Microwave imaging .....	6
<b>1.4 THESIS STRUCTURE</b> .....	8
<b>2. THEORETICAL FOUNDATION</b> .....	9
<b>2.1 MAXWELL’S EQUATIONS AND ELECTRICAL NETWORKS</b> .....	9
<b>2.2 PROBLEM DESCRIPTION</b> .....	11
2.2.1 Reconstruction methods for Microwave Imaging .....	12
<b>2.3 DBIM-TwIST</b> .....	14
2.3.1 Debye Model .....	15
2.3.2 Finite-Difference Time-Domain Method (FDTD) .....	16
2.3.3 Image Reconstruction Quality .....	17
2.3.4 FDTD Implementation in Multiple Grid Resolutions .....	18
2.3.5 Convergence Optimization.....	19

Optimized Initial Guess .....	19
Multiple Frequency Optimization .....	19
L <sup>1</sup> Norm Regularization .....	19
2.3.6 Blocks Diagram .....	21
2.4 CSI-FEM .....	22
2.4.1 Problem Formulation.....	22
2.4.2 Finite Element Method Discretization .....	24
2.4.3 The Inversion Algorithm .....	25
2.4.4 Initializing Algorithm.....	27
2.4.5 Image Reconstruction Quality.....	28
2.4.6 Multiplicative regularization (MR) .....	28
2.4.7 Blocks Diagram .....	29
3. ALGORITHMS COMPARISON .....	30
3.1 ANTENNA BEHAVIOUR.....	31
3.2 MATERIALS AND DEBYE PARAMETERS .....	34
3.3 TYPE OF COMPARISON .....	37
Validation model .....	37
Simulation model .....	37
3.4 MODEL 1.....	39
3.4.1 ALGORITHMS VALIDATION .....	39
• DBIM-TwIST .....	39
• CS .....	41
3.4.2 ALGORITHMS PERFORMANCE WITH SIMULATION DATA.....	43
• DBIM-TwIST .....	44
• CS .....	48
3.5 MODEL 2.....	49
3.5.1 ALGORITHMS VALIDATION .....	50
• DBIM-TwIST .....	50
• CS .....	52
3.5.2 ALGORITHMS SIMULATION .....	53
• DBIM-TwIST .....	54
• CS .....	59
3.5.3 SUMMARY .....	60

4. EXPERIMENTAL TESTING .....	61
4.1 MICROWAVE IMAGING SYSTEM .....	61
4.2 MEASUREMENTS PROCESSING.....	64
4.3 EXPERIMENTAL RESULTS.....	65
4.3.1 Case 1 .....	66
• DBIM-TwIST .....	67
• CS .....	69
4.3.2 Case 2 .....	71
• DBIM-TwIST .....	71
• CS .....	73
4.3.3 Case 3 .....	74
• DBIM-TwIST .....	75
• CS .....	76
4.3.4 SUMMARY .....	77
5. CONCLUSIONS AND FUTURE DEVELOPMENTS .....	78

# List of Figures

Figure 1: Ischemic stroke representation [2] .....	2
Figure 2: Haemorrhagic stroke representation [2].....	2
Figure 3: Computerized Tomography device [4]. .....	3
Figure 4: Magnetic Resonance device [6]. .....	4
Figure 5: The Stroke Finder antennas helmet of Chalmers University [14].....	7
Figure 6: Two-port device and relevant power waves.....	10
Figure 7: Typical scenario of a microwave imaging. $\Omega$ domain contains all the system and D domain encloses reconstructed area. OI is the object of interest. ....	12
Figure 8: Kane S. Yee lattice used for Maxwell's equation discretization .....	16
Figure 9: 5(a) Pareto curve, 5(b) Pareto curve with log-log scale [18]. .....	20
Figure 10: DBIM-TwIST Flowchart (N=number of iterations) .....	21
Figure 11: CS Flowchart (N= number of iterations) .....	29
Figure 12: Two models used for algorithms comparison. On right, blood phantom immersed in the coupling medium. On left, blood phantom in a brain phantom immersed in the coupling medium. ....	30
Figure 13: Relative permittivity and conductivity of the coupling medium [7].....	31
Figure 14: RX/TX antenna; (a) top side; (b) bottom side [7].....	32
Figure 15: model created with the external software in order to study antenna behaviour. In the model there is an antenna immersed in the coupling medium (Triton and water mixture).....	32
Figure 16: Reflection coefficient amplitude of the antenna immersed in the coupling medium. ....	33
Figure 17: Dielectric properties fitting of background medium (Triton/water). ....	36
Figure 18: Geometry of model 1, realised with a CAD software .....	39
Figure 19: Matlab model, created with FDTD method .....	40
Figure 20: DBIM-TwIST reconstructions of electric properties. On left $\epsilon_r$ distribution, on right $\sigma$ distribution. ....	40
Figure 21: On left Relative error, on right Residual at each iteration .....	41
Figure 22: Matlab model, created with FEM of CS .....	41
Figure 23: CS reconstructions of electric properties. On left $\epsilon_r$ distribution, on right $\sigma$ distribution.....	42
Figure 24: Cost functional at each iteration.....	42

Figure 25: Simulation model, created with a CAD software. On left model without blood target, on right model with blood target. ....	43
Figure 26: Electric field distribution when only an antenna is on. The intensity scale on right is in dB. ....	43
Figure 27: DBIM-TwIST reconstructions of electric properties. On left $\epsilon_r$ distribution, on right $\sigma$ distribution. ....	44
Figure 28: Residual at each iteration. ....	45
Figure 29: Module trend for each radiating antenna ( $f=1.2$ GHz).....	46
Figure 30: Phase trend for each radiating antenna ( $f=1.2$ GHz).....	47
Figure 31: CS reconstructions of electric properties. On left $\epsilon_r$ distribution, on right $\sigma$ distribution.....	48
Figure 32: Cost functional at each iteration.....	49
Figure 33: Geometry of model 2, realised with a CAD software.....	49
Figure 34: Matlab model, created with Finite difference time domain method.....	50
Figure 35: DBIM-TwIST reconstructions of electric properties. On left $\epsilon_r$ distribution, on right $\sigma$ distribution. ....	51
Figure 36: On left Relative error, on right Residual at each iteration.....	51
Figure 37: Matlab model, created with FEM of CS.....	52
Figure 38: CS reconstructions of electric properties. On left $\epsilon_r$ distribution, on right $\sigma$ distribution.....	52
Figure 39: Cost functional at each iteration.....	53
Figure 40: Simulation model, created with a CAD software. On left model without blood target, on right model with blood target. ....	53
Figure 41: Electric field distribution when only an antenna is on. The intensity scale on right is in dB. ....	54
Figure 42: DBIM-TwIST reconstructions of electric properties. On left $\epsilon_r$ distribution, on right $\sigma$ distribution. ....	54
Figure 43: Residual at each iteration. ....	55
Figure 44: DBIM-TwIST reconstructions of dielectric properties for the iteration with minimum residual. On left $\epsilon_r$ distribution, on right $\sigma$ distribution. ....	56
Figure 45: Module trend for each radiating antenna ( $f=1.1$ GHz).....	57
Figure 46: Phase trend for each radiating antenna ( $f=1.1$ GHz).....	58
Figure 47: CS reconstructions of electric properties. On left $\epsilon_r$ distribution, on right $\sigma$ distribution.....	59
Figure 48: Cost functional at each iteration.....	59
Figure 49: Instrumentation block diagram.....	61
Figure 50: Realized microwave imaging system [7]......	62
Figure 51: Tank filled with the coupling liquid with phantom and RX/TX antennas inside [7]......	63
Figure 52: Phantom; (a) top view, (b) side view, (c) inserted cylinders [7]......	63

Figure 53: Measures with the VNA.....	64
Figure 54: De-embedding operation on the Scattering matrix .....	64
Figure 55: the three geometries used for algorithms comparison when the input are measured data. In each model there is blood phantom immersed in the coupling medium. From left to right, there are case 1, case 2 and case 3. ....	66
Figure 56: Geometry in case 1.....	66
Figure 57: DBIM-TwIST results in case 1, with a frequency equal to 1 GHz. First column: raw data (25 iterations), second column: raw data with de-embedding (35 iterations), third column: raw data with Time Gating (50 iterations), fourth column: raw data with de-embedding and TG (25 iterations). First row: $\epsilon\mathbf{r}$ , second row: $\sigma$ . ....	67
Figure 58: DBIM-TwIST reconstructions of electric properties without the contributions of neighbouring antennas. Input data: raw data with TG. On left $\epsilon\mathbf{r}$ distribution, on right $\sigma$ distribution. ....	68
Figure 59: Residual at each iteration .....	68
Figure 60: CS results in case 1, with a frequency equal to 1 GHz. First column: raw data (10 iterations), second column: raw data with de-embedding (10 iterations), third column: raw data with Time Gating (10 iterations), fourth column: raw data with de-embedding and Time Gating (10 iterations). First row: $\epsilon\mathbf{r}$ , second row: $\sigma$ . ....	69
Figure 61: CS reconstructions of electric properties without the contributions of neighbouring antennas. Input data: raw data with TG. On left $\epsilon\mathbf{r}$ distribution, on right $\sigma$ distribution. ....	70
Figure 62: Cost functional at each iteration.....	70
Figure 63: Geometry in case 2.....	71
Figure 64: DBIM-TwIST reconstructions of electric properties without the contributions of neighbouring antennas. Input data: raw data with TG. On left $\epsilon\mathbf{r}$ distribution, on right $\sigma$ distribution. ....	71
Figure 65: DBIM-TwIST reconstructions of electric properties without the contributions of neighbouring antennas. Input data: raw data with TG. On left $\epsilon\mathbf{r}$ distribution, on right $\sigma$ distribution. ....	72
Figure 66: Residual at each iteration .....	73
Figure 67: CS reconstructions of electric properties without the contributions of neighbouring antennas. Input data: raw data with TG. On left $\epsilon\mathbf{r}$ distribution, on right $\sigma$ distribution. ....	73
Figure 68: Cost functional at each iteration.....	74
Figure 69: Geometry in case 3.....	74
Figure 70: DBIM-TwIST reconstructions of electric properties without the contributions of neighbouring antennas. Input data: raw data with TG. On left $\epsilon\mathbf{r}$ distribution, on right $\sigma$ distribution. ....	75
Figure 71: Residual at each iteration. ....	76

Figure 72: CS reconstructions of electric properties without the contributions of neighbouring antennas. Input data: raw data with TG. On left  $\epsilon_r$  distribution, on right  $\sigma$  distribution..... 76

Figure 73: Cost functional at each iteration..... 77

# List of Tables

Table 1: PROS and CONS of different imaging techniques .....	5
Table 2: Dielectric properties of brain tissues in 1.0 GHz, official CNR website [10]..	6
Table 3: Classes of image reconstruction algorithms [3]. .....	13
Table 4: Electric properties of model materials in the frequencies range. ....	35
Table 5: Debye parameters in the range from 1.0 to 1.5 GHz (with $\tau=5.3505 \cdot 10 - 7$ s). .....	36
Table 6: Comparison between expected and obtained electric properties values .....	40
Table 7: Comparison between expected and obtained electric properties values. ....	42
Table 8: Comparison between expected and obtained electric properties values. ....	44
Table 9: Comparison between expected and obtained electric properties values. ....	48
Table 10: Comparison between expected and obtained electrical properties values....	51
Table 11: Comparison between expected and obtained electrical properties values....	53
Table 12: Comparison between expected and obtained electrical properties values....	55
Table 13: Comparison between expected and obtained electrical properties values....	59
Table 14: Comparison between expected and obtained electrical properties values....	68
Table 15: Comparison between expected and obtained electrical properties values....	72
Table 16: Comparison between expected and obtained electrical properties values....	72
Table 17: Comparison between expected and obtained electrical properties values....	74
Table 18: Comparison between expected and obtained electrical properties values....	75
Table 19: Comparison between expected and obtained electrical properties values....	77

# Glossary

- BCs** Boundaries Conditions
- CNR** Consiglio Nazionale delle Ricerche
- CS** Contrast Source
- CT** Computerized Tomography
- DBIM** Distorted Born Iterative Method
- DUT** Device Under Test
- FD-CSI** Finite Difference Contrast Source Inversion method
- FDTD** Finite Difference Time Domain
- FEM** Finite Element Method
- IE** Integral Equation
- MR** Multiplicative Regularization
- MRI** Magnetic Resonance Imaging
- MWI** MicroWave Imaging
- OI** Object of Interest
- PDE** Partial Differential Equation
- TG** Time Gating
- TSVD** Truncated Singular Value Decomposition
- TwIST** Two-step Iterative Shrinkage/Thresholding method
- VNA** Vector Network Analyzer

# 1. INTRODUCTION

## 1.1 STROKE AND IMAGING METHODS

The stroke is one of the most common cardiovascular diseases, in fact it has an incidence of around 15 million cases each year all over the world. There are two main type of stroke: ischemic, when a brain vessel is clogged, and hemorrhagic, when a brain vessel bursts. In both, the poor blood flow leads to cells death [1].

Different symptoms appear after a brain stroke, for example dizziness, inability to feel or move one part of the body, loss of vision to one side, speaking or understanding problems. These symptoms can be permanent, instead if they last for less than one or two hours it is a mini-stroke or transient ischemic attack [1].

High pressure is the main risk factor for stroke, but there are other risk factors such as diabetes mellitus, atrial fibrillation, high blood cholesterol, obesity and tobacco smoking. Nowadays, in some parts of the world, stroke rehabilitation takes place in stroke units [1].

### 1.1.1 *Ischemic stroke*

As mentioned above, ischemic stroke is caused by a loss of blood supply to part of the brain. One of its main causes is atherosclerosis, it leads to blood vessels lumen narrow and therefore to blood flow reduction. When there are emboli in the circulatory system, for example in the heart (caused by an atrial fibrillation), they can block brain blood vessels. In general, ischemic stroke can be treated with a medication that breaks the clot (but only if it is detected within three to four and half hours) [1].

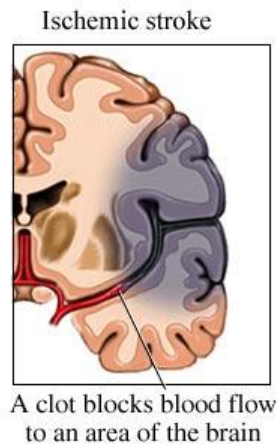


**Figure 1: Ischemic stroke representation [2]**

### 1.1.2 Hemorrhagic stroke

As mentioned above, a hemorrhagic stroke occurs when blood vessels breaks and the blood goes in the surrounding tissues. This type of stroke can be caused by three main factors:

- Aneurism: a part of the blood vessel swells and sometimes it breaks;
- Arteriovenous malformation: irregular blood vessels shape;
- High blood pressure, sometimes it results in bleeding into the brain.

Only some hemorrhagic strokes can be treated and in general patient undergoes surgery [1].

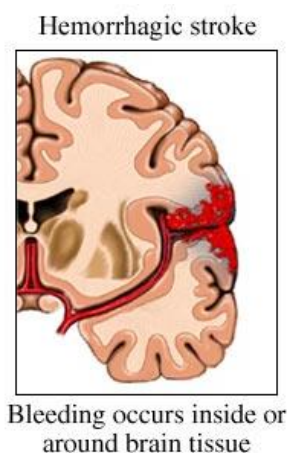


**Figure 2: Haemorrhagic stroke representation [2].**

## 1.2 TECHNIQUES FOR STROKE IMAGING

Clinicians must intervene in different ways in dependence on the type of stroke. A wrong therapy can lead to patient death. Moreover, intervention rapidity is fundamental for the therapy effectiveness, so the diagnostic methodologies have an important role of support to clinicians in choosing the therapy.

Nowadays, the most common techniques are X-ray computerized tomography (CT) and Magnetic Resonance Imaging (MRI). These techniques are explained and analyzed in the following sections.

### *X-Rays*

X-Rays is one of the first imaging technique, it is a form of electromagnetic radiation, with a frequency range from  $3 \cdot 10^{16}$  Hz to  $3 \cdot 10^{19}$  Hz (wavelength range from 0.01 nm to 10 nm).

X-rays beam travels in a straight line through the body and the resulting image (2D with a traditional radiology device or 3D with a Computerized Tomography device) is the model of the total attenuation. For instance, bones look white on the radiography because of the presence of calcium, which absorbs X-rays the most, instead lungs look black because air absorbs least.

The drawback of this technique is invasiveness, especially if it is repeated several times. On the other hand, it has a relatively low cost if compared with other imaging techniques [3].



**Figure 3: Computerized Tomography device [4].**

## *Magnetic Resonance Imaging (MRI)*

Magnetic Resonance Imaging uses radiofrequency pulses in the range of frequency from 1 to 100 MHz. There is a strong magnetic field on the tissues, and the protons of water molecules align with the direction of this field. Then an electric field is applied, and its photons are absorbed by the aligned protons. After that the electric field is turned off and the protons return to the low energy state emitting a photon, which is captured by the scanner. The reconstruction of the image is based on the fact that protons return at their equilibrium state with different rates, this difference can be detected [3].

This kind of technique has different drawbacks: it is expensive, time consuming and unsuited for claustrophobic patients, for continuous monitoring in ambulance or for at bedside [5].



**Figure 4: Magnetic Resonance device [6].**

## 1.3 INNOVATIVE TECHNIQUE FOR STROKE IMAGING: MICROWAVE IMAGING (MWI)

An interesting alternative is Microwave Imaging. The future objective is to monitor post-stroke evolution of a bedridden patient in real time, so the device characteristics should be: low cost, small size, low intensity, non-ionizing radiations. The Microwave imaging technique has all these features [7].

The fundamental concept is that microwaves are sensitive to dielectric contrast and thanks to the difference between tissues and abnormal blood flow (stroke case), it's possible to classify stroke types and also to obtain quantitative parameters [8], [9].

This kind of technique provides complementary information to existing medical imaging methods.

It has a lot of advantages, for instance it can penetrate through light opaque materials except conductors, it is harmless at controlled level because it has not thermal or ionizing effects and technological cost is acceptable.

On the other hand, unfortunately it has low spatial resolution, scattering effect, the extraction of relevant data is very complex, and results is dependent from scenario [7].

Table 1 shows advantages and drawbacks of the three first mentioned techniques.

	<b>X-ray CT</b>	<b>MRI</b>	<b>MWI</b>
<b>PROS</b>	<ul style="list-style-type: none"> <li>• Fast in creating the image</li> <li>• Relatively low cost</li> </ul>	<ul style="list-style-type: none"> <li>• Non-ionizing</li> </ul>	<ul style="list-style-type: none"> <li>• Low cost</li> <li>• Non-ionizing</li> <li>• Non-contacting</li> <li>• Portable</li> </ul>
<b>CONS</b>	<ul style="list-style-type: none"> <li>• Ionizing</li> <li>• Uncomfortable compressions</li> <li>• Not portable</li> </ul>	<ul style="list-style-type: none"> <li>• High cost</li> <li>• Not portable</li> <li>• Claustrophobia, long acquisition time</li> <li>• Detection depends on the absorption of contrast agent (if needed)</li> </ul>	<ul style="list-style-type: none"> <li>• Under development</li> <li>• No clinical experience</li> </ul>

**Table 1: PROS and CONS of different imaging techniques**

The subsequent parts deal with principles and reconstruction methods of microwave imaging technique.

### 1.3.1 Principles of Microwave imaging

Microwave imaging technique can be used to recognize different brain tissues, but also to take over the presence of stroke. The stimulus is sent through an antenna array located around the object of interest and the frequency radiation is in the range of microwave (300 MHz-300 GHz).

Thanks to the low intensity of the radiation, this device is considered safe. It was thought for the monitoring of bedridden patients, but also for the first diagnosis in ambulance, in fact it has small size and it can be portable [5].

The device is composed by power supply and processing blocks connected to an antennas helmet through a switch matrix. In chapter 4.1 each part of the system is described.

The field is measured through the same antennas and it's called total field, instead the field measured when there isn't the target is called incident field. The scattered field is the difference between the total and the incident one. Thanks to this difference it's possible to obtain dielectric properties distribution by solving the problem with an inverse algorithm. Thanks to the dielectric properties difference between tissues and abnormal blood flow (stroke case), it's possible to classify stroke types and to obtain quantitative parameters. Table 2 shows the different brain regions in terms of dielectric permittivity and conductivity for a frequency in the range of interest: 1.0 GHz.

Tissue name	Conductivity [S/m]	Relative permittivity
Brain Gray matter	0.985	52.282
Brain White matter	0.622	38.577
Cerebrospinal Fluid	2.455	68.439
Bone Cortical	0,156	12.363
Bone Cancellous	0,364	20.584
Blood	1.583	61.065

**Table 2: Dielectric properties of brain tissues in 1.0 GHz, official CNR website [10].**

In recent years, more and more research groups work on microwave imaging device.

At first, the studies focused on breast cancer imaging, in fact dielectric characterization shows an important contrast between healthy and malignant tissues. Only after the attention is shifted to the brain imaging (for stroke, cancerous tumours and haemorrhages caused by trauma).

Amin M. Abbosh et al. [11] proposed a portable microwave head imaging system using a Software-Defined Radio and a switching network. It is portable, highly compact, low cost and feasible for time-critical applications.

Another important contribute is given by Christian Pichot et al., who demonstrated the possibility to detect simulated hemorrhagic strokes with microwave systems. The synthetic data are obtained through electromagnetic simulations with a realistic brain model corrupted with noise [12].

A patient with stroke needs to be treated as soon as possible, the rapidity of intervention can prevent death or serious disabilities. Depending on the type of stroke (ischemic or hemorrhagic), the therapy is different; for this reason the team of Chalmers University [13] developed the “Stroke Finder”, a device for faster diagnostics. It is able to distinct an ischemic from an hemorrhagic stroke.

Figure 5 shows the antennas helmet designed by the Chalmers team.

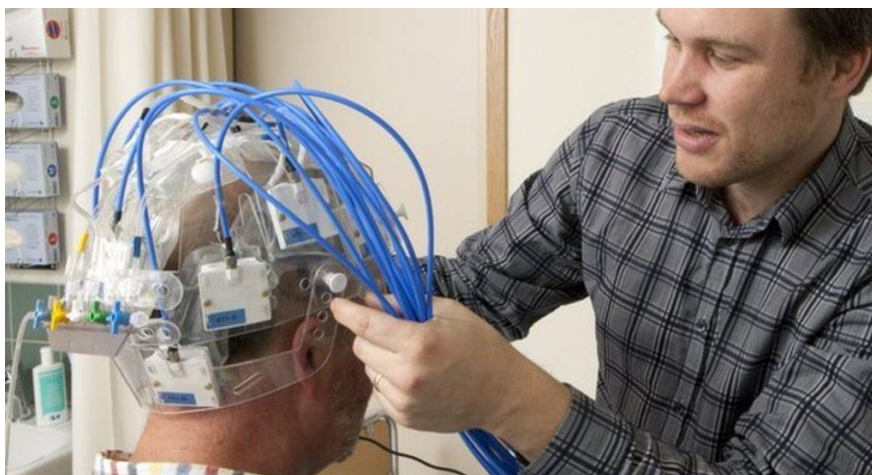


**Figure 5: The Stroke Finder antennas helmet of Chalmers University [14]**

## 1.4 THESIS STRUCTURE

In chapter 2, after a brief introduction of theoretical foundation with Maxwell's equations and some important network parameters, there is the description of the problem with the typical scenario of microwave imaging.

After, the different typologies of reconstruction algorithms for microwave imaging are presented and there are also the descriptions of the two algorithms treated in this thesis: the Distorted Born iterative method (DBIM) and the Contrast source method (CS).

In chapter 3, two models are used for algorithms validation. Besides, with the same models, simulated data are created. Algorithms performances are compared in both validation and simulation.

In chapter 4, there is the description of laboratory instrumentation, and the presentation of algorithms performances with measured data with three different models.

Finally, in chapter 5, there is a summary of the obtained results and considerations about algorithms with possible future developments and improvements.

## 2. THEORETICAL FOUNDATION

Microwaves are a kind of electromagnetic radiation with a frequency between 300 MHz and 300 GHz (wavelengths in a range from about 1 mm to 1 m) [15]. They can penetrate inside objects and in this way it's possible to obtain information on an invisible object located inside an opaque one. For this reason, it can be very useful in biomedical applications, in which the most famous microwave technique is tomography.

In this chapter, there are some fundamental concepts of electromagnetic, problem presentation and description of all the algorithms steps.

### 2.1 MAXWELL'S EQUATIONS AND ELECTRICAL NETWORKS

The problems of electromagnetism can be solved with Maxwell's equations. In particular, these equations describe the relationships between the sources ( $\mathbf{J}(\mathbf{r},t)$ ) and four field vectors that constitute these kind of problems: electric fields  $\mathbf{E}(\mathbf{r},t)$ , magnetic fields  $\mathbf{H}(\mathbf{r},t)$ , electric induction  $\mathbf{D}(\mathbf{r},t)$  and magnetic induction  $\mathbf{B}(\mathbf{r},t)$ .

$$\nabla \times \mathbf{E}(\mathbf{r}, t) = -\frac{\partial \mathbf{B}(\mathbf{r}, t)}{\partial t} \quad (1)$$

$$\nabla \times \mathbf{H}(\mathbf{r}, t) = \frac{\partial \mathbf{D}(\mathbf{r}, t)}{\partial t} + \mathbf{J}_c(\mathbf{r}, t) + \mathbf{J}(\mathbf{r}, t) \quad (2)$$

Maxwell's equations must be accompanied by relations that describe the connection between inductions and fields:

$$\mathbf{B}(\mathbf{r}, t) = \mu \mathbf{H}(\mathbf{r}, t) \quad (3)$$

$$\mathbf{D}(\mathbf{r}, t) = \varepsilon \mathbf{E}(\mathbf{r}, t) \quad (4)$$

With

$$\mu = \mu_0 \mu_r \quad (5)$$

$$\varepsilon = \varepsilon_0 \varepsilon_r \quad (6)$$

Where

- $\mu_0 = 4\pi \cdot 10^{-7} \text{ H/m}$
- $\varepsilon_0 = \frac{1}{\mu_0 c^2} \approx \frac{1}{36\pi} \cdot 10^{-9} \text{ F/m}$

$\mu_r$  and  $\varepsilon_r$  are the relative permittivity and permeability respectively. Moreover, when dielectric contains free charges,  $\mathbf{J}_c(\mathbf{r}, t)$  rises with the presence of an electric field [16].

An important parameter to describe electrical network, is the Scattering parameters (elements of S matrix). In order to explain S meaning, a two port device is considered (Figure 6).

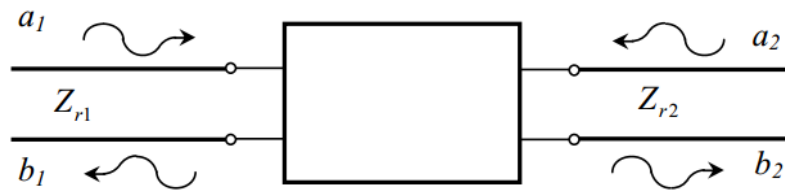


Figure 6: Two-port device and relevant power waves

On this line,  $a_i$  and  $b_i$  are power waves, and  $Z_{ri}$  (reference impedance) that is the characteristic impedance of a transmission line connected to port  $i$ . In the case of two-port device, the following relations can be defined [16]:

$$\begin{cases} b_1 = S_{11}a_1 + S_{12}a_2 \\ b_2 = S_{21}a_1 + S_{22}a_2 \end{cases} \quad (7)$$

The relations can be written in matrix form:

$$[b] = [S][a] \quad (8)$$

“Where  $[S]$  is a 2x2 complex matrix. Obviously, the equation 8 is valid also in the case of a N-port network. [...] The terms on the main diagonal (as  $S_{11}$ ) are the reflection

coefficients at a port when all the others are terminated with the reference impedance” as reported in Lecture Notes on Transmission Line Theory [16]. During the thesis, there are a lot of references to this parameter.

Another way to characterize an electrical network is through Transmission matrix [T], it relates two sides of a structure in the power wave basis. The forward and backward power waves are related to the incident and scattered ones, as reported in equation 9 [16].

$$\begin{aligned} [c_1^+] &= [a_1] & [c_2^+] &= [b_2] \\ [c_1^-] &= [b_1] & [c_2^-] &= [a_2] \end{aligned} \quad (9)$$

The characterization of the two-port device through the Transmission matrix is the following:

$$\begin{cases} c_1^+ = T_{11}c_2^+ + T_{12}c_2^- \\ c_1^- = T_{21}c_2^+ + T_{22}c_2^- \end{cases} \quad (10)$$

Or in matrix form [13]:

$$[c_1] = [T][c_2] \quad (11)$$

## 2.2 PROBLEM DESCRIPTION

MWI, as considered here, has the goal to quantitatively reconstruct electric properties of an object of interest (OI). The OI is surrounded by a background medium with known electrical properties. The reconstruction domain is surrounded by an antenna array, each antenna radiates sequentially one at a time, and the total field is measured on each antenna (also in the transmitter). When there isn't the object of interest in the background medium, the measured field is called Incident field. Figure 7 shows the geometry of the two-dimensional model.

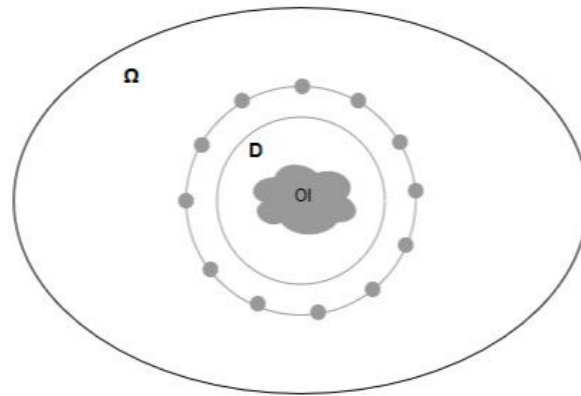


**Figure 7: Typical scenario of a microwave imaging.  $\Omega$  domain contains all the system and  $D$  domain encloses reconstructed area.  $OI$  is the object of interest.**

### 2.2.1 Reconstruction methods for Microwave Imaging

The reconstruction algorithms for microwave imaging can be divided into two big classes: **Linear (model-based) inversion methods** and **Non-linear (iterative) methods**.

These two kinds of algorithms solve an inverse scattering problem to obtain dielectric properties in the region of interest, in fact they are also known as inverse scattering methods.

- **Linear (model-based) inversion methods:** they are based on Born approximation and they have a low computational cost; indeed, the processing is simple and robust. If the targets have low contrast, it's possible to obtain a quantitative reconstruction with this kind of algorithm.
- **Iterative algorithms:** the iterative scheme consequence is the high computational cost. This kind of algorithm needs of a priori information, mostly if there is a regularization scheme. Convergence strongly depends on the choice of the parameters and noisy.[3].

<b>TOMOGRAPHIC IMAGING</b>	
<b>Iterative algorithms</b>	<b>Linear inversion algorithms</b>
Requires to solve an inverse scattering problem to obtain the dielectric properties of the body under test	
Iterative scheme	First order Born approximation
High computational cost	Low computational cost
Quantitative reconstructions in general cases	Qualitative reconstruction
Need of a priori information, convergence strongly depends on the choice of the parameters, sensitivity to noise	Simple, robust signal processing

**Table 3: Classes of image reconstruction algorithms [3].**

An example of linear inversion algorithm is Truncated Singular Value Decomposition (TSVD) [17]; in order to evaluate the evolution of the stroke, TSVD considers two different times; in fact, the input of this algorithm is the difference between scattering matrices measured at these two times. It obtains qualitative information about the target: presence, position and shape.

There are different inverse scattering methods, for example the Distorted Born iterative method (DBIM), that at each iteration calls a forward solver to compute the scattered fields or the Contrast Source inversion method (CS), which searches electrical properties minimizing a cost functional. In this thesis, these two kinds of non-linear reconstruction algorithm are compared.

To better confront the two algorithms (the CS and the DBIM), the performances are analysed with the same model and in the same conditions. In fact, in both algorithms the domain is approximated to an unbounded region, applying absorbing boundary conditions to the outer lattice to simulate the extension of the lattice to infinity.

## 2.3 DBIM-TwIST

The Distorted Born iterative method (DBIM) evaluates the distribution of dielectric permittivity in the region of interest by solving an electromagnetic inverse scattering problem. “Under the Born approximation, a linear integral equation at each iteration can be discretized for all transmit-receive pairs, leading to a linear system that can be solved by various methods including the TwIST method”, as described from Zhenzhuang Miao and Panagiotis Kosmas in [18]. This method is used to solve the linear equations set and it computes the current iteration using the two previous ones. The TwIST method is characterized by more accurate reconstructions and faster convergence compared to one step iterative methods. The DBIM method is based on a non-linear integral equation, its 2-D scalar form is reported in the following equation:

$$E_s(\mathbf{r}_n, \mathbf{r}_m) = E(\mathbf{r}_n, \mathbf{r}_m) - E_b(\mathbf{r}_n, \mathbf{r}_m) = \omega^2 \mu \int G_b(\mathbf{r}_n, \mathbf{r}) E(\mathbf{r}, \mathbf{r}_m) (\varepsilon(\mathbf{r}) - \varepsilon_b(\mathbf{r})) d\mathbf{r} \quad (12)$$

where,

- $E$ , total field;
- $E_s$ , scattered field;
- $E_b$ , background field;
- $\mathbf{r}_n$ , transmitting antenna location;
- $\mathbf{r}_m$ , receiving antenna location;
- $\varepsilon(\mathbf{r})$  object's complex permittivity;
- $\varepsilon_b(\mathbf{r})$  background's complex permittivity;
- $G_b$ , Green's function for the background medium;
- $\mu$ , permeability;
- $\omega = 2\pi f$ , angular frequency.

The total field is known only in antenna locations where it is measured. The difference between  $\varepsilon(\mathbf{r})$  e  $\varepsilon_b(\mathbf{r})$  is updated at each iteration.

The TwIST goal is to estimate an unknown vector  $\mathbf{x}$  (original image) from an observation vector  $\mathbf{y}$ , which are linked by the linear equation below.

$$\mathbf{y} = A\mathbf{x} \quad (13)$$

The iterative equations used in the TwIST algorithm are [15]:

$$\mathbf{x}_{t+1} = (1 - \alpha)\mathbf{x}_{t-1} + (\alpha - \beta)\mathbf{x}_t + \beta\Gamma_\lambda(\mathbf{x}_t) \quad (14)$$

$$\Gamma_\lambda(\mathbf{x}) = \psi_\lambda(\mathbf{x} + A^T(\mathbf{y} - A\mathbf{x})) \quad (15)$$

where,

- $\alpha$  and  $\beta$ , TwIST parameters;
- $\psi_\lambda$ , denoising function that is a regularization function and  $\lambda$  is a weighting parameter [19].

As we can see, the next estimate ( $\mathbf{x}_{t+1}$ ) depends on the previous ( $\mathbf{x}_{t-1}$ ) and the current solution ( $\mathbf{x}_t$ ). By adjusting the TwIST parameters it's possible to change robustness and convergence speed of the algorithm [18], [20].

### 2.3.1 Debye Model

The algorithm uses the Debye model to describe the dielectric permittivity trend as a function of frequency. According to this model, the complex dielectric constant is:

$$\varepsilon_r(\omega) = \varepsilon_\infty + \frac{\varepsilon_s - \varepsilon_\infty}{1 + j\omega\tau} - j \frac{\sigma_s}{\omega\varepsilon_0} \quad (16)$$

Where,

- $\varepsilon_r$  is relative permittivity
- $\varepsilon_s = \varepsilon_r(\omega \rightarrow 0)$
- $\varepsilon_\infty = \varepsilon_r(\omega \rightarrow \infty)$
- $\sigma_s = \sigma(\omega \rightarrow 0)$ , is electrical conductivity
- $\tau$ , relaxation time for the material

At frequency  $\omega\tau=1$  (relaxation frequency), half molecules can align to external E-field. The Debye model imaginary part contains two contributions: permittivity and conductivity. Biological tissues have losses for conduction (motion of free charges) and polarization (dipoles rotate to align to the applied E-field and these rotations dissipate energy) [21].

### 2.3.2 Finite-Difference Time-Domain Method (FDTD)

The DBIM-TwIST algorithm exploits the Finite-Difference Time-Domain Method as resolution method for electromagnetic problem. The basic idea is to discretize the Maxwell's equations both in time and space, as the name suggests, it approximates derivative to finite difference.

Kane S. Yee was the first to define a fields discretization scheme and to solve Maxwell's equations numerically. Field components are calculated in different positions, therefore it's possible a separate calculation of magnetic and electric fields.

He defined a lattice that shows the different locations of field components. Nowadays, this lattice is always used when model is discretized for FDTD calculation [19].

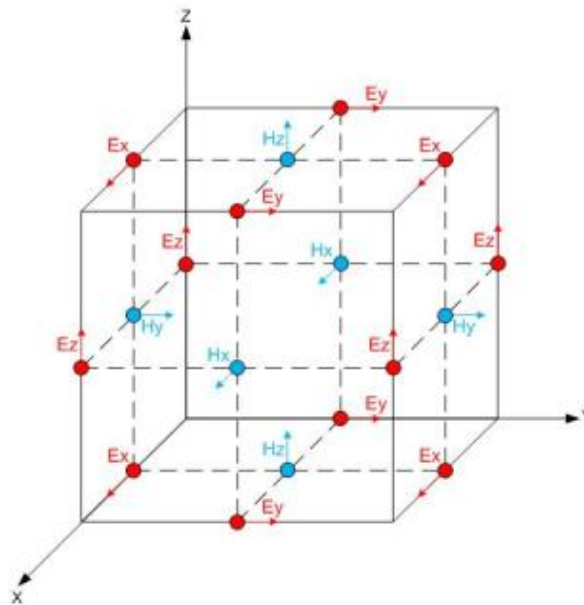


Figure 8: Kane S. Yee lattice used for Maxwell's equation discretization

Once can notice, electric field components (red circle) are calculated in the middle of the edge instead magnetic field components (blue circle) are calculated in the middle of surface.

Maximum time-step must guarantee with the following inequality:

$$\Delta t \leq \frac{1}{u \sqrt{\frac{1}{(\Delta x)^2} + \frac{1}{(\Delta y)^2} + \frac{1}{(\Delta z)^2}}} \quad (17)$$

Where  $u$  is the velocity propagation and  $\Delta x$ ,  $\Delta y$  e  $\Delta z$  are the spatial dimensions of the smallest element in the simulation grid [19], [22], [23].

### 2.3.3 Image Reconstruction Quality

To analyze algorithm performance, at each iteration, a relative error is calculated:

$$\text{"Relative error"} = \frac{\|\varepsilon_{\infty}^t \text{ original} - \varepsilon_{\infty}^t \text{ reconstructed}\|^2}{\|\varepsilon_{\infty}^t \text{ original}\|^2} \quad (18)$$

Where,

- $t$ , iteration number
- $\|\cdot\|$ ,  $L^2$  norm

The definition for the norm is:  $\|\cdot\|_p = ((\sum_n |\cdot|^p))^{1/2}$ .

In this case,  $\varepsilon_{\infty}$  is reported, but the same metric can be used for each Debye parameter. In order to have a direct comparison with realistic application, a Residual error is used ( $\varepsilon_{\infty}$  cannot be known in a realistic application):

$$\text{Residual} = \|M_t^E - M_t^S\| \quad (19)$$

Where,

- $M_t^E$ , complex vector of the experimental data at  $t_{th}$  iteration, in the antenna positions;
- $M_t^S$ , complex vector of the model data at  $t_{th}$  iteration, in the antenna locations.

This residual difference is calculated at each iteration and it could be a stopping criterion [18].

### 2.3.4 FDTD Implementation in Multiple Grid Resolutions

The possible resolution values are from 0.5 mm to 2 mm with a step of 0.5 mm (maximum value must be smaller than the skin thickness). Obviously, the resolution choice changes data of FDTD forward solver, in fact sampling frequency (for simulation data) depends on the inverse of  $\Delta t$ , which in turn depends on the spatial increment ( $\Delta x = \Delta y$ ):

$$\Delta t = \Delta x / (2 * c) \quad (20)$$

With  $c$  the speed of light in vacuum.

In the algorithm, a soft source excitation is applied. It exploits a current source to obtain a field.

$$\mathbf{E}_{n+1} = \mathbf{E}_n + source(n) \quad (21)$$

Where  $source(n)$  is a voltage source discrete series. In different time step there is successive accumulation of energy thanks to soft source. Simulated sources are compensated in respect of the chosen resolution for the relation between  $\Delta t$  and  $\Delta x$ . Therefore, parameter  $mul$  is defined as the ratio between multiple resolution and original resolution:

$$mul = \frac{r_c}{0.5 \text{ mm}} \quad (22)$$

$$\Delta t = \Delta x / (2 * c) / mul \quad (23)$$

$$source_m = source_0 / mul^2 \quad (24)$$

Where,

- $r_c$ , targeted resolution;
- $source_0$ , original excitation signal;
- $source_m$ , modified source [18].

### 2.3.5 Convergence Optimization

In the algorithm there are different techniques to obtain an optimized convergence:

- method to estimate the initial guess;
- use multi-frequency data to improve algorithm performance;
- $L^1$  norm regularization based on the Pareto curve.

Each mentioned techniques are explained in the successive subsections, even if in this thesis the results are obtained without convergence optimization [18].

#### *Optimized Initial Guess*

DBIM is an iterative local optimization method and, as all this type of methods, it is sensitive to the initial guess. A suitable initial guess can reduce computational time, speed up convergence and also it can increase the algorithm stability. In biomedical applications, there are very little information known *a priori*, and finding an accurate initial guess is difficult. In the presented DBIM-TwIST algorithm, the estimation of initial condition is based on two assumptions:

- Region of interest is homogeneous and filled with normal tissue. DBIM-TwIST is run for a determined number of iterations;
- This process is repeated for different Cases, in which the algorithm adopts different dielectric properties (into normal tissues range);
- The algorithm chooses the case that minimizing the data residual [18].

#### *Multiple Frequency Optimization*

The algorithm resolution and robustness can be improved using more than one frequency. There are different ways to exploit multi-frequency data. In this algorithm there are a single frequency reconstruction, but the dielectric properties given as input, in the current frequency, depend from the output of the previous one [18].

#### *$L^1$ Norm Regularization*

The TwIST algorithm provides sparse solution of the Linear Inverse Problem, therefore it can be regularized with tools used in other sparse-algorithm, an example is

the Basis Pursuit (BP) problem. BP goal is to find a sparse solution of  $Ax=b$  ( $A$  is a matrix  $m \times n$  and  $b$  a vector  $m \times 1$ ).

When  $m \ll n$  the problem is ill-posed. One of the approaches is to solve:

$$\min_x \|x\|_1 \text{ s.t. } Ax = b \quad (25)$$

Obviously, because of the presence of noise and imperfect data, it is impossible to fit the exact linear system. Another formulation with L1 norm regularized least-squares problem is:

$$\min_x \|Ax - b\|_2^2 + \lambda \|x\|_1 \quad (26)$$

Calling  $x_\lambda$  the optimal solution of the equation 27, the minimal residual (of the same equation) for each  $\lambda \geq 0$  is given by:

$$\Phi(\lambda) = \|Ax_\lambda - b\|_2 \quad (27)$$

The Pareto curve is the method used to find the optimal value of  $\lambda$ . This method finds a good compromise between minimizing L1 norm of the solution  $x$  and L2 norm of the residual [18].

Figure 9 shows the Pareto curve (a) and Pareto curve in log-log scale (b). The last one is used to determine the optimal value of the L1 regularization parameter  $\lambda$  ( $\lambda_{opt}$ ), that corresponds to the maximum slope.

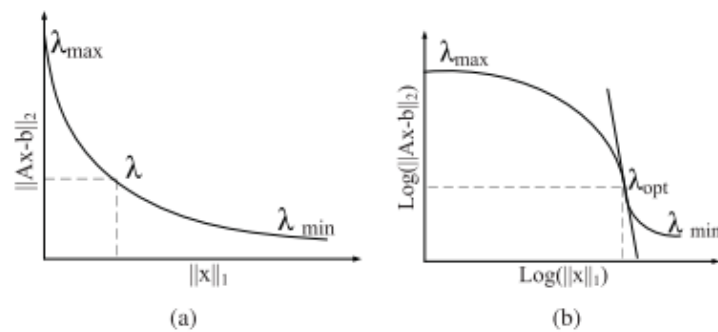


Figure 9: 5(a) Pareto curve, 5(b) Pareto curve with log-log scale [18].

To reduce the number of  $\lambda$  values, it is chosen with this equation:

$$\lambda(n) = \|A^T b\|_\infty \cdot \delta^n \quad n \in \mathbf{Z}^+ \quad (28)$$

Here,  $\delta$  is a decreasing factor with a range from 0.1 to 1.

- $\delta \rightarrow 1$ , more accurate Pareto curve;
- $\delta \rightarrow 0.1$ , a smaller number of values [18].

### 2.3.6 Blocks Diagram

The Blocks Diagram of DBIM-TwIST algorithm is shown below, with related legend:

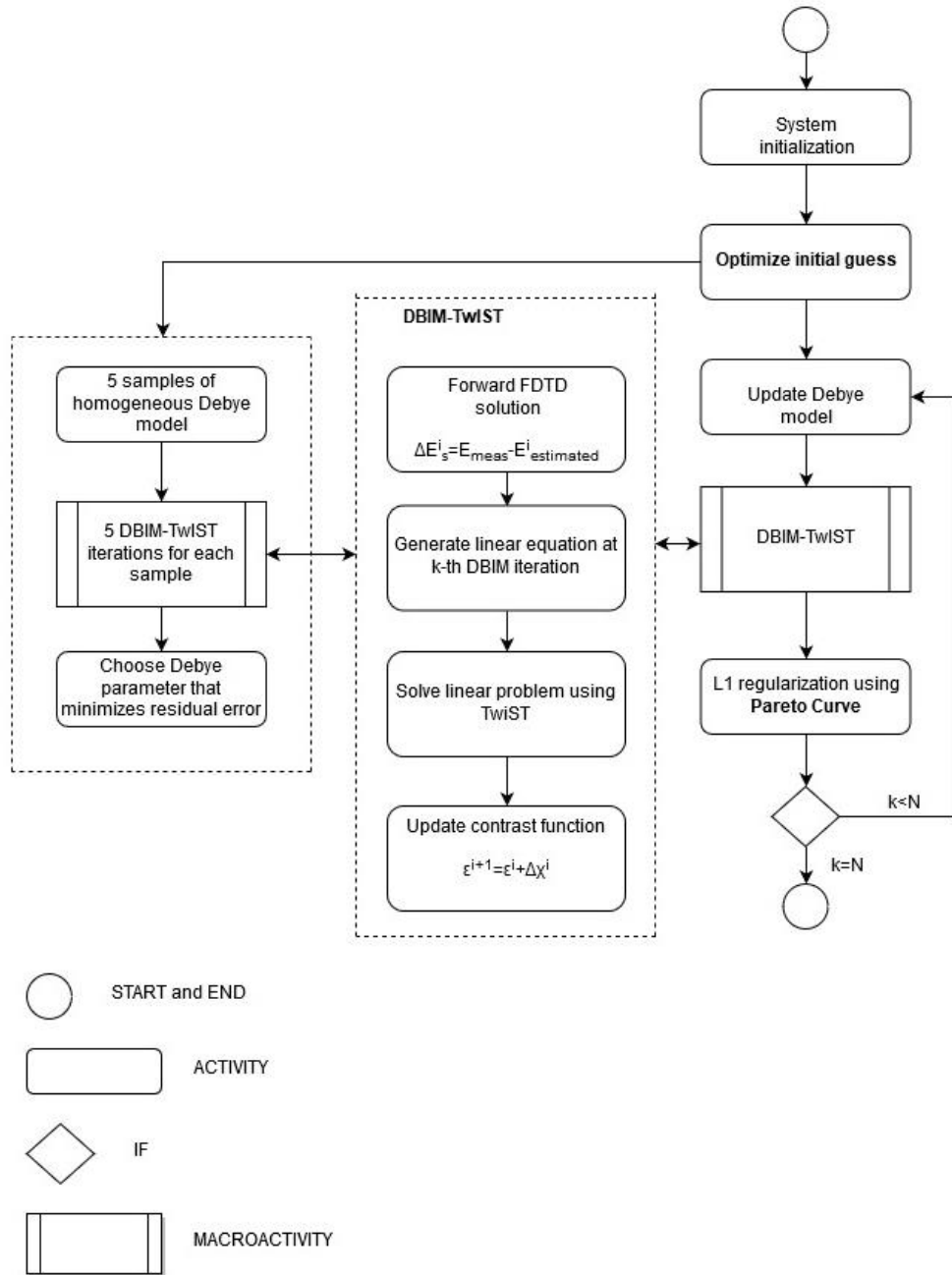


Figure 10: DBIM-TwIST Flowchart (N=number of iterations)

## 2.4 CSI-FEM

Contrast Source Inversion method (CSI) is one of the most successful techniques for solving inverse scattering problems without calling a forward solver at each iteration.

In fact, in this algorithm the inverse problem isn't solved at each iteration, but two variables are update with the conjugate gradient method. These two variables are contrast and contrast sources, and the update has the purpose to minimize the cost functional.

In the contrast source, the integral Equation (IE) formulation is often used for a lot of applications, but this kind of formulation is efficient if the domain can be approximated to unbounded and if the background medium is homogeneous.

To overcome these limitations, a new formulation is developed: Finite Difference CSI (FD-CSI). This algorithm uses a structured, uniform discretization grid of the Helmholtz Partial differential equation (PDE). That grid allows to have inhomogeneous background and different type of boundary conditions [24], [25], [26], [27].

However, it has two great drawbacks: the rectangular grid impedes arbitrary shape modelling and the insertion of a priori information about the target becomes difficult because in general it requires the insertion of parameters in irregular shape regions.

A FEM discretization of PDE allows to overcome these limits. It uses an unstructured and non-uniform mesh that allows to improve reconstruction in an adaptive way, where it is necessary. Thanks to it the boundary can be of any type and shape [28], [29].

### 2.4.1 Problem Formulation

The unknown object of interest is in the domain  $D$ , and electrical properties of the background medium are known. The electric contrast is reported in equation 29:

$$\chi(\mathbf{r}) = \frac{\varepsilon_r(\mathbf{r}) - \varepsilon_b(\mathbf{r})}{\varepsilon_b(\mathbf{r})} \quad \text{with} \quad \chi(\mathbf{r}) = 0 \text{ for } \mathbf{r} \notin D \quad (29)$$

With,

- $\mathbf{r} = (x, y)$ , position vector (2D);
- $\varepsilon_r(\mathbf{r})$  complex relative permittivity;

- $\varepsilon_b(\mathbf{r})$  background complex relative permittivity.

Transmitter are modelled as 2D point sources, that radiate one at a time. The incident field (field measured when there isn't the object of interest) is modelled with Helmholtz scalar equation:

$$\nabla^2 E_t^{inc}(\mathbf{r}) + k_b^2(\mathbf{r})E_t^{inc}(\mathbf{r}) = j\omega\mu_0 J_t(\mathbf{r}) \quad (30)$$

Where,

-  $\omega = 2\pi f$  , angular frequency

-  $k_b(\mathbf{r}) = \omega\sqrt{\mu_0\varepsilon_0\varepsilon_b(\mathbf{r})}$  , background wavenumber

-  $J_t(\mathbf{r}) = \frac{-1}{j\omega\mu_0} \delta(\mathbf{r} - \mathbf{r}_t)$ , is the source term (for transmitter t in position  $\mathbf{r}_t$ )

When the OI is in the reconstruction region, the measured field satisfied the same equation:

$$\nabla^2 E_t(\mathbf{r}) + k^2(\mathbf{r})E_t(\mathbf{r}) = j\omega\mu_0 J_t(\mathbf{r}) \quad (31)$$

Where,  $k(\mathbf{r}) = \omega\sqrt{\mu_0\varepsilon_0\varepsilon_r(\mathbf{r})}$  is the wavenumber.

Here, the contrast source variables is defined. It represents sources terms that depend on total field.

$$\omega_t(\mathbf{r}) \hat{=} \chi(\mathbf{r})E_t(\mathbf{r}) \quad (32)$$

The equation 33 defines the scattered field as difference between total and incident field [28]:

$$E_t^{sct}(\mathbf{r}) \hat{=} E_t(\mathbf{r}) - E_t^{inc}(\mathbf{r}) \quad (33)$$

$$\nabla^2 E_t^{sct}(\mathbf{r}) + k_b^2(\mathbf{r})E_t^{sct}(\mathbf{r}) = -k_b^2(\mathbf{r})\omega_t(\mathbf{r}) \quad (34)$$

### 2.4.2 Finite Element Method Discretization

The domain mesh is composed by first order triangular elements, and it has  $N$  nodes. Each node has a basis function that depends only on geometry mesh. Standard Rayleigh-Ritz formulation is used for discretization and this kind of formulation produces the follow matrix equation [28]:

$$[\mathbf{S} - \mathbf{T}_b]E_{t,\Omega}^{sct}(\mathbf{r}) = \mathbf{T}_b\omega_{t,\Omega} \quad (35)$$

With,

- $\mathbf{S} \in \mathbb{C}^{N \times N}$ , stiffness matrix (depends on BCs)
- $\mathbf{T}_b \in \mathbb{C}^{N \times N}$ , mass matrix correlated to background medium properties
- $E_{t,\Omega}^{sct} \in \mathbb{C}^N$  vector that contains scattered field at each node
- $\omega_{t,\Omega} \in \mathbb{C}^N$  vector that contains the contrast source corresponding to transmitter  $t$ .

Considering the  $i$ th row and  $j$ th column:

$$S_{i,j} = \int_{\Omega} \nabla \lambda_i \cdot \nabla \lambda_j ds \quad \text{and} \quad T_{bi,j} = \sum_{p=1}^N \int_{\Omega} k_{b,p}^2 \lambda_i \lambda_j \lambda_p ds \quad (36)$$

Where,

- $\lambda_i, \lambda_j, \lambda_p$  linear basis functions ( $i$ th,  $j$ th and  $p$ th node)
- $\nabla$ , spatial gradient operator
- $k_{b,p}$ , background wavenumber at node  $p$

Moreover, in FEM-CSI algorithm, several matrix operators are used:

- $\mathbf{M}_S \in \mathbb{C}^{R \times N}$ , transforms field values of  $N$  nodes into field values of receiver;
- $\mathbf{M}_D \in \mathbb{C}^{R \times N}$ , selects field values of  $I$  nodes in the domain  $D$  (reconstruction region)

- $\mathbf{L} \in \mathbb{C}^{N \times I}$ , provides scattered field values, given the contrast source variable as reported in the equation 35 [28].

$$E_{t,\Omega}^{sct} = \mathbf{L}[\omega_t] = (\mathbf{S} - \mathbf{T}_b)^{-1} \mathbf{T}_b \mathbf{M}_D^T[\omega_t] \quad (37)$$

### 2.4.3 The Inversion Algorithm

The CSI algorithm purpose is to minimize the cost functional, updating two variables: contrast and source contrast sequentially. The functional cost is composed by two part: data error ( $F^S$ ) and object error ( $F^D$ ):

$$F(\chi, \omega_t) = F^S(\omega_t) + F^D(\chi, \omega_t) = \quad (38)$$

$$\frac{\sum_t \|f_t - \mathbf{M}_S \mathbf{L}[\omega_t]\|_S^2}{\sum_t \|f_t\|_S^2} + \frac{\sum_t \|\chi \otimes E_t^{inc} - \omega_t + \chi \otimes \mathbf{M}_D \mathbf{L}[\omega_t]\|_D^2}{\sum_t \|\chi \otimes E_t^{inc}\|_D^2}$$

- $f_t \in \mathbb{C}^R$ , measured scattered field data for each transmitter at R receiver locations
- $\chi \in \mathbb{C}^I$ , contrast vector for nodes located inside D
- $E_t^{inc} = \mathbf{M}_D[E_{t,\Omega}^{inc}]$ , is the incident field vector for nodes inside D corresponding to t transmitter
- $a \otimes b$  is the Hadamard product

In the first step of the algorithm the contrast variable  $\chi$  is constant, instead contrast source variables  $\omega_t$  is updated using conjugate-gradient (CG) method with Polak-Ribière search directions.

In the second step  $F^D(\chi, \omega_t)$  is minimized, keeping constant  $\omega_t$ .

The equation for the first step is:

$$\omega_{t,n} = \omega_{t,n-1} + \alpha_{t,n} d_{t,n} \quad (39)$$

where,

- n is the iteration number
- $d_{t,n}$  are Polak-Ribère search directions

- $\alpha_{t,n}$  is the update step-size and it is determined as:

$$\alpha_{t,n} = \arg \min_{\alpha} \{F(\omega_{t,n-1} + \alpha_{t,n} d_{t,n}, \chi_{n-1})\} \quad (40)$$

Setting the derivative of  $F(\omega_{t,n-1} + \alpha_{t,n} d_{t,n}, \chi_{n-1})$  with respect to  $\alpha_{t,n}$  equal to zero, a closed expression can be found:

$$\alpha_{t,n} = \frac{\eta^S \langle \rho_{t,n-1}, \mathbf{M}_S \mathbf{L}[d_{t,n}] \rangle_S + \eta_n^D \langle r_{t,n-1}, d_{n,t} - \chi_{n-1} \otimes \mathbf{M}_D \mathbf{L}[d_{t,n}] \rangle_D}{\eta^S \|\mathbf{M}_S \mathbf{L}[d_{t,n}]\|_S^2 + \eta_n^D \|d_{n,t} - \chi_{n-1} \otimes \mathbf{M}_D \mathbf{L}[d_{t,n}]\|_D^2} \quad (41)$$

Here the error terms  $\rho_{t,n-1}$  and  $r_{t,n-1}$  are:

$$\rho_{t,n-1} = f_t - \mathbf{M}_S \mathbf{L}[\omega_{t,n-1}] \quad (42)$$

$$r_{t,n-1} = \chi_{n-1} \otimes E_t^{inc} - \omega_{t,n-1} + \chi_{n-1} \otimes \mathbf{M}_D \mathbf{L}[\omega_{t,n-1}] \quad (43)$$

and the normalization factors are:

$$\eta^S = (\sum_t \|f_t\|_S^2)^{-1} \quad (44)$$

$$\eta_n^D = (\sum_t \|\chi_{n-1} \otimes E_t^{inc}\|_D^2)^{-1} \quad (45)$$

The directions are calculated with the following formula:

$$d_{t,n} = -g_{t,n} + \frac{\langle g_{t,n}, g_{t,n} - g_{t,n-1} \rangle_D}{\|g_{t,n-1}\|_D^2} d_{t,n-1} \quad (46)$$

In which  $g_{t,n}$  is the cost function gradient  $F(\chi, \omega_t)$  with respect to the contrast sources given by:

$$g_{t,n} = -2\eta^S \mathbf{T}_D^{-1} \mathbf{L}^H \mathbf{M}_S^H \rho_{t,n-1} - 2\eta_n^D \mathbf{T}_D^{-1} (\mathbf{I} - \mathbf{L}^H \mathbf{M}_D^T \mathbf{X}_{n-1}^H) \mathbf{T}_D r_{t,n-1} \quad (47)$$

Where,

- $\mathbf{I} \in \mathbb{R}^{I \times I}$ , identity matrix
- $\mathbf{X}_{n-1} = \text{diag}(\chi_{n-1})$ , diagonal matrix

Once assessed the contrast source variable, contrast  $\chi$  is calculated minimizing the modified domain equation  $F_m^D(\chi)$  that is reported evaluated in equation 48:

$$F_m^D(\chi) = \sum_t \|\chi \otimes E_t^{inc} - \omega_t + \chi \otimes \mathbf{M}_D \mathbf{L}[\omega_t]\|_D^2 \quad (48)$$

In this algorithm step,  $\omega_t$  is considered constant. For each iteration n:

$$(\sum_t \mathbf{E}_{t,n}^H \mathbf{T}_D \mathbf{E}_{t,n}) \chi_n = \sum_t \mathbf{E}_{t,n}^H \mathbf{T}_D \omega_{t,n} \quad (49)$$

Here,  $\mathbf{E}_{t,n} \in \mathbb{C}^{I \times I}$  is the total field diagonal matrix, in which the diagonal terms are [28]:

$$\mathbf{E}_{t,n} = E_t^{inc} + \mathbf{M}_D \mathbf{L}[\omega_{t,n}] \quad (50)$$

#### 2.4.4 Initializing Algorithm

The initial guess is evaluated minimizing  $F_s(\omega_t)$  (cost functional calculated as error in data equation) with the steepest descent method.

$$\omega_{t,n} = \frac{\text{Re}\langle \mathbf{M}_S \mathbf{L}[\mathbf{G}^S f_t], f_t \rangle_S}{\|\mathbf{M}_S \mathbf{L}[\mathbf{G}^S f_t]\|_S^2} \mathbf{G}^S f_t \quad (51)$$

With,

$$\mathbf{G}^S = -2\eta^S \mathbf{T}_D^{-1} \mathbf{L}^H \mathbf{M}_S^H \quad (52)$$

With the equation (49) the variable X is evaluated and  $d_{t,0}$  is set to zero [28].

### 2.4.5 Image Reconstruction Quality

In order to quantify the image reconstruction quality, a relative error between the reconstructed image and the exact image is evaluated, through equation 53 [28].

$$E_{RR} = \frac{|\varepsilon_{exact}(r) - \varepsilon_{reconstruct}(r)|_D}{|\varepsilon_{exact}(r)|_D} \quad (53)$$

### 2.4.6 Multiplicative regularization (MR)

An optimization method, often used with various inversion algorithms including CSI, is Multiplicative Regularization (MR). The addition of this multiplicative term improves the algorithm performance also with noisy measurements data. In particular, with this term, the functional cost becomes:

$$F_n(\underline{\chi}, \underline{\bar{\omega}}_t) = F_n^{MR}(\underline{\chi}) \times F^{CSI}(\underline{\chi}, \underline{\bar{\omega}}_t) \quad (54)$$

Where  $F_n^{MR}$  (multiplicative regularization term) is calculated with:

$$F_n^{MR}(\underline{\chi}) = \int_D \underline{b}_n^2 (|\nabla \underline{\chi}|^2 + \delta_n^2) dr \quad (55)$$

In which,

$$\underline{b}_n = \sqrt{(A(|\nabla \underline{\chi}_{n-1}|^2 + \delta_n^2))^{-1}} \quad (56)$$

$$\delta_n^2 = F^D(\underline{\chi}_n^{CSI}, \underline{\bar{\omega}}_{t,n}) \bar{A}^{-1} \quad (57)$$

Here

- $A$ , total area in the domain  $D$ ;
- $\bar{A}$ , mean area of the triangles in the domain  $D$ .

In this thesis, all the tests are done without Multiplicative regularization method [30].

### 2.4.7 Blocks Diagram

The Blocks Diagram of CS algorithm is shown below, with related legend:

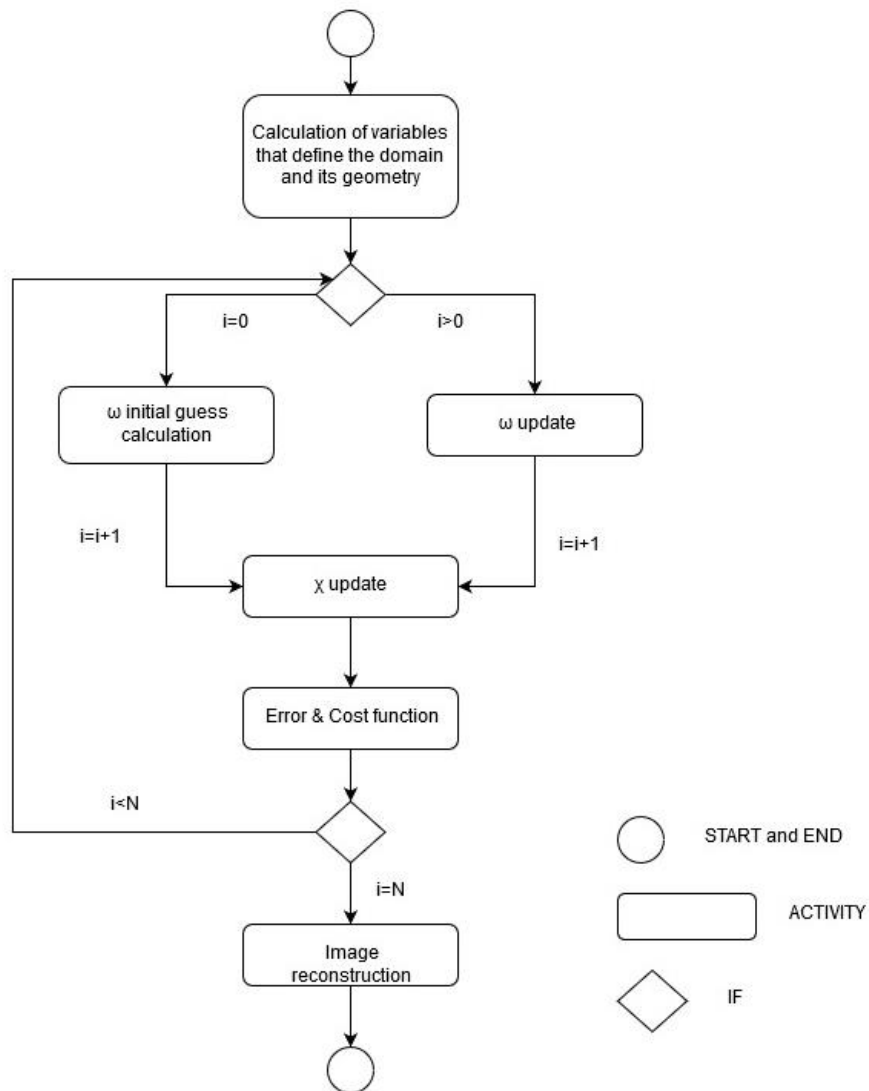


Figure 11: CS Flowchart (N= number of iterations)

### 3. ALGORITHMS COMPARISON

In this chapter, there is the comparison between the DBIM and the CS algorithm performances in the case of interest: brain reconstruction and stroke identification and monitoring.

In the first part there is the analysis of the best work frequency range with the study of the antenna resonance. After that, there is the comparison through two models:

- 1) Blood phantom immersed in the background medium and surrounded by twelve antennas;
- 2) Brain phantom immersed in the background medium and surrounded by twelve antennas. In the brain phantom there is the blood target.

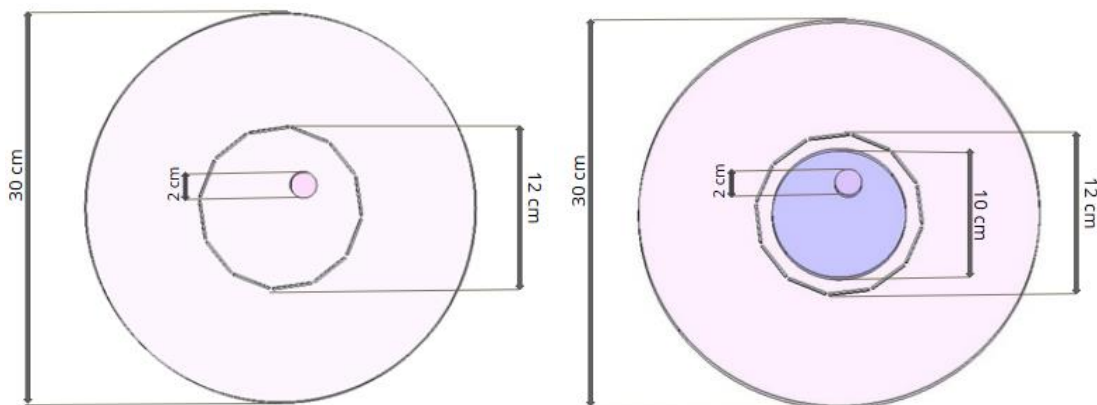


**Figure 12: Two models used for algorithms comparison. On right, blood phantom immersed in the coupling medium. On left, blood phantom in a brain phantom immersed in the coupling medium.**

For each model, there are two types of analyses:

- **Validation:** algorithms performance when input models are created with the same mechanism of image reconstruction. In particular, for the DBIM-TwIST algorithm there is a model created in Matlab with Finite Difference Time Domain Method, instead for the CS algorithm there is a model creates always in

Matlab with the FEM inside the CS; both the models are 2D. This section is the closest to the ideal case.

- **Simulation:** algorithms performance with data calculated in a 3D simulation realized with two software: CAD-mesh software for creation of the model (geometry, materials, conditions) and the mesh and an in-house FEM for evaluation of the antennas S parameters. This case is closer to the reality than the previous one because the sources are modelled as antennas and not as point sources and it is a 3D model (the geometry of domain, brain phantom and blood target is a cylinder).

### 3.1 ANTENNA BEHAVIOUR

Before proceeding with comparison, it's important to understand antenna behaviour when it's immersed in the background medium.

The coupling medium is a compound of Triton X-100 and water with a volume percentage of 70/30, it is “very stable in time and easy to prepare (the two liquids are simply mixed together at room temperature). Moreover, the corresponding attenuation in the considered frequency band is much lower than other mixtures proposed in literature, allowing to work with less noisy measurements” [7].

Figure 13 shows trend of coupling medium conductivity and relative permittivity as a function of frequency.

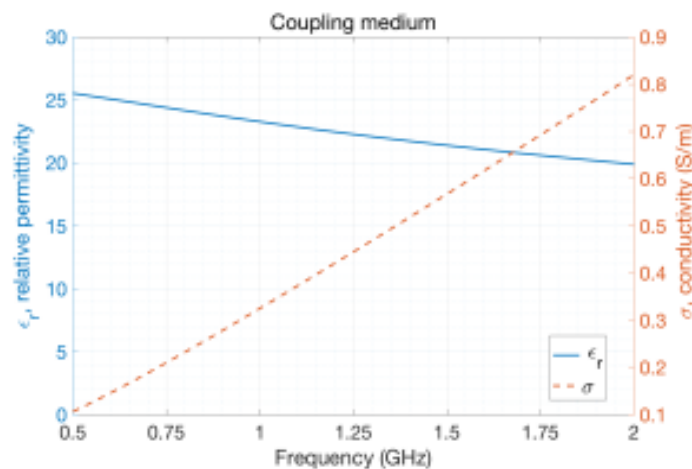


Figure 13: Relative permittivity and conductivity of the coupling medium [7].

The microwave imaging system has wide-band monopole antennas (an example is shown in Figure 14).

It is printed on a FR4 dielectric substrate with a thickness of 1.6 mm, instead on the top side there is a transmission line ended with a triangular shape radiating part with a double stub matching circuit. The ground plane on the bottom side terminates at the beginning of the radiating triangle [7].

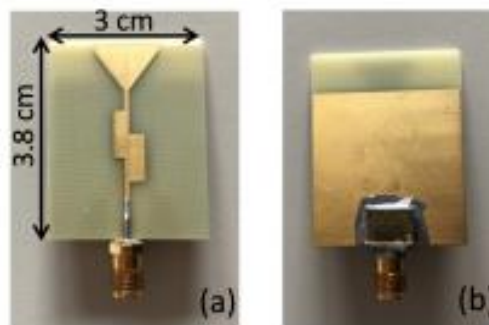


Figure 14: RX/TX antenna; (a) top side; (b) bottom side [7].

In Figure 15 there is the model used to simulate the antenna behaviour when it is immersed in the background medium.

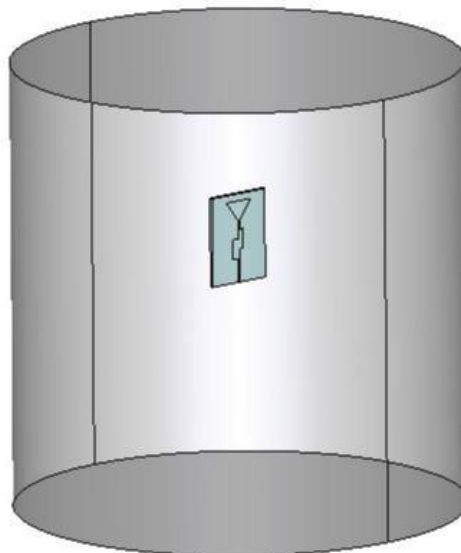
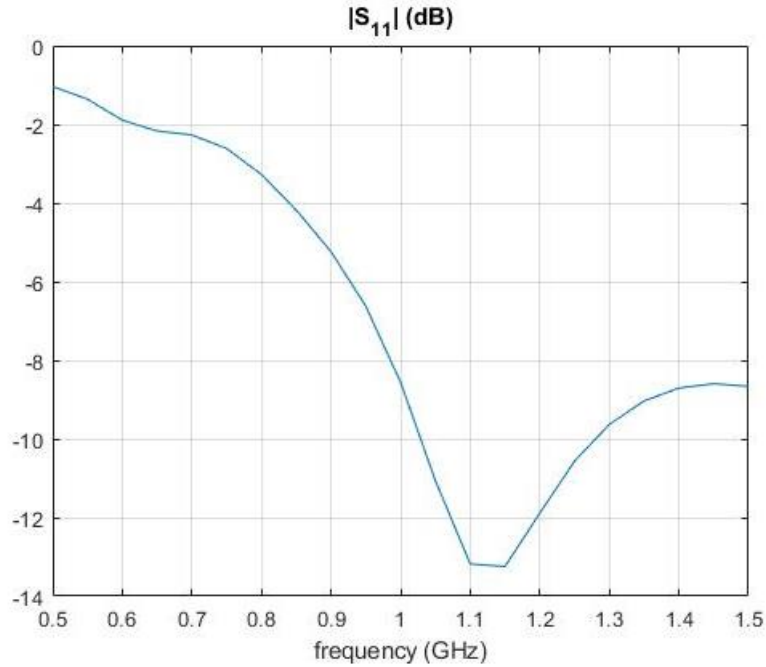


Figure 15: model created with the external software in order to study antenna behaviour. In the model there is an antenna immersed in the coupling medium (Triton and water mixture)

This part is fundamental to choose the best work frequencies. The analysis is made in the range from 0.5 to 1.5 GHz with a step of 0.05 GHz.

Figure 16 shows  $S_{11}$  trend as a function of frequency.



**Figure 16: Reflection coefficient amplitude of the antenna immersed in the coupling medium.**

One can notice that the resonance frequency is on 1.10 and 1.15 GHz. In equation 58 is reported the relation that links wavelength to relative permittivity and frequency.

$$\lambda = \frac{c}{f\sqrt{Real(\epsilon_r)}} \quad (58)$$

Where,

- $c=299\ 792\ 458$  m/s, is light speed;
- $\epsilon_r$ , relative permittivity;
- $f$ , frequency

In this case,  $f=1.1$  GHz and  $Real(\epsilon_r) = 22.7$

$$\lambda = \frac{299\,792\,458 \text{ m/s}}{1.1 \cdot 10^9 \sqrt{22.7}} = 0.057 \text{ m} \quad (59)$$

Mesh discretization, used in the CAD mesh software for simulation, depends on wavelength.

For example, in this work maximum tetrahedron dimension is chosen for background ( $l_{b\_max}$ ) as a tenth of lambda and for reconstruction area ( $l_{ra\_max}$ ) as a twentieth of lambda.

$$l_{b\_max} = \frac{\lambda}{10} = 5.7 \text{ mm} \quad (60)$$

$$l_{ra\_max} = \frac{\lambda}{20} = 2.9 \text{ mm} \quad (61)$$

For each model the best frequency has been searched in the range from 1.0 GHz to 1.5 GHz (with a step of 0.1 GHz), because the presence of other model components can shift slightly the resonance frequency.

## 3.2 MATERIALS AND DEBYE PARAMETERS

In Table 4 are reported the electric properties of materials concerned in the chosen range (1.0-1.5 GHz).

<b>Material</b>	$\epsilon_r$	$\sigma$ (S/m)	<b>Frequency (GHz)</b>
<b>Triton 70</b>	23.00	0.33	1.0
	22.70	0.38	1.1
	22.40	0.43	1.2
	22.1	0.48	1.3
	21.8	0.53	1.4
	21.5	0.58	1.5
<b>Blood</b>	63.41	1.58	1.0
	63.06	1.62	1.1
	62.81	1.67	1.2
	62.70	1.75	1.3
	62.62	1.81	1.4
	62.35	1.89	1.5
<b>Brain</b>	42.78	0.75	1.0
	42.31	0.80	1.1
	41.90	0.86	1.2
	41.77	0.92	1.3
	41.71	0.98	1.4
	41.47	1.05	1.5

**Table 4: Electric properties of model materials in the frequencies range.**

As mentioned above, the DBIM exploits Debye parameters to describe dielectric properties as function of frequency. They are derived by curve-fitting data from experimental measurements. In particular, for the background medium, Debye parameters are calculated in a range from 1 GHz to 3 GHz; instead, for Brain and for blood the trend is more complicated to fit so the Debye parameters are calculated in a

narrower range, from 1.0 GHz to 1.5 GHz. In Figure 17, the fitting of the Background medium is reported as example.

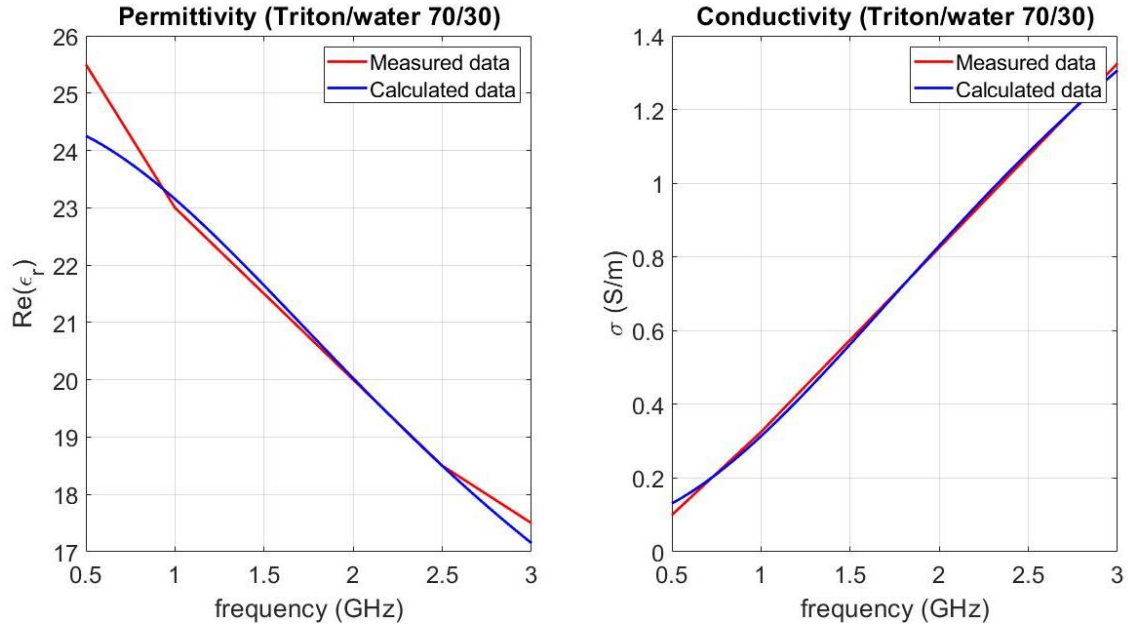


Figure 17: Dielectric properties fitting of background medium (Triton/water).

In Table 5 are reported Debye parameters of background medium, brain and blood for the range 1.0 GHz to 1.5 GHz.

Medium	$\epsilon_{\infty}$	$\Delta\epsilon$	$\sigma_s$ (S/m)
Triton/water	9.7650	14.9000	0.0634
Brain	25.5000	19.3000	0.4100
Blood	48.2000	16.9000	1.3000

Table 5: Debye parameters in the range from 1.0 to 1.5 GHz (with  $\tau=5.3505 \cdot 10^{-7}$ s).

### 3.3 TYPE OF COMPARISON

As said previously, there are two types of comparison for each model. Starting from the simplest case and coming to the most complex one, it's possible to understand the algorithms problems and their causes.

In this part, there is a description of each comparison method, and after that there is the analysis of algorithms performance with 2 models.

#### *Validation model*

This comparison allows to analyse each part of the two algorithms, in fact also the input data are created with DBIM and CS. Both the algorithms create the model in Matlab with the same geometry and materials, but with a different mechanism because DBIM works with FDTD, instead CS is based on FEM.

There are several reasons because this model is distant from reality:

- Antennas are modelled as point sources (great approximation);
- The model is 2 D;
- The mechanism used for model creation is the same used for image reconstruction.

For these reasons, the results are better than with other input data, but this case is the furthest from reality.

#### *Simulation model*

In this section, algorithms input data are obtained through simulations.

Geometry, materials, conditions and excitations are created with an external software.

Maxwell's equations are solved with an in-house FEM (FEM\_POLITO).

At the end of the simulation, FEM\_POLITO returns electric and magnetic field distributions (module and phase) and S parameters; the latter are used as input for the algorithms.

The models are realized in 3D, and in this case the sources aren't point sources (as in the first comparison) but are created as antennas. For these two reasons, this case is closer to reality than the previous one.

In this type of comparison, calibration is fundamental. It consists of a regularization of simulated data through a comparison with reference values. Calibration method is equal in the two algorithms and it is described in equation 63 and 64.

$$|E_{with\ target}^{calibrated}|_{dB} = |S_{with\ target}^{sim}|_{dB} - |S_{not\ target}^{sim}|_{dB} + |E_{not\ target}^{ref}|_{dB} \quad (62)$$

$$Pha(E_{with\ target}^{calibrated}) = Pha(S_{with\ target}^{sim}) - Pha(S_{not\ target}^{sim}) + Pha(E_{not\ target}^{ref}) \quad (63)$$

With:

- $Pha$  operator extrapolates the phase of its argument;
- $E_{with\ target}^{calibrated}$ , reflected field when object of interest is in reconstruction area;
- $S_{with\ target}^{sim}$ , simulated data when object of interest is in reconstruction area;
- $S_{not\ target}^{sim}$ , simulated data when object of interest isn't in reconstruction area;
- $E_{not\ target}^{ref}$ , incident field (no object in reconstruction area). It is calculated in the algorithms (DBIM and CS).

This type of calibration is described in [31], [32] and it allows to delete each error that are constant in the two simulation data ( $S_{not\ target}^{sim}$  and  $S_{with\ target}^{sim}$ ).

### 3.4 MODEL 1

This first model consists of a cylinder blood phantom immersed in a coupling medium and surrounded by twelve antennas. The Figure 18 shows the geometry of the model.

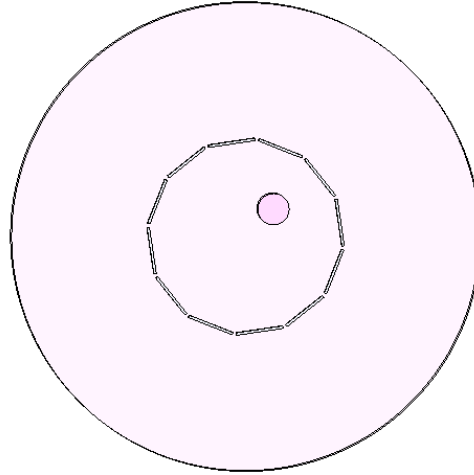


Figure 18: Geometry of model 1, realised with a CAD software

#### 3.4.1 ALGORITHMS VALIDATION

In this section, there is the algorithms validation. Models for validation are created in Matlab for both the algorithms. In the first part, there is the validation of the DBIM algorithm, with input model, reconstructed variables ( $\epsilon_r$  and  $\sigma$ ), relative error (equation 18) and residual (equation 19). In the second part, there is the validation of CS algorithm, with input model, reconstructed variables ( $\epsilon_r$  and  $\sigma$ ) and cost functional.

- *DBIM-TwIST*

Algorithm settings:

- Work frequency: 1.1 GHz
- Number of iterations: 75
- Resolution of the reconstructed image: 2 mm

In the Figure 19, there is the model created in Matlab.

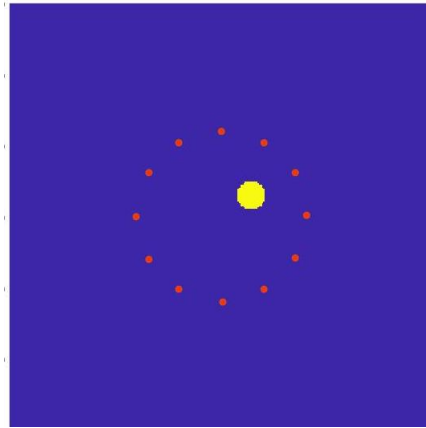


Figure 19: Matlab model, created with FDTD method

Figure 20 shows the reconstructions of the electric properties. In this case the DBIM algorithm works very well: the position and dimension of the target are right and variables values are very close to the expected ones.

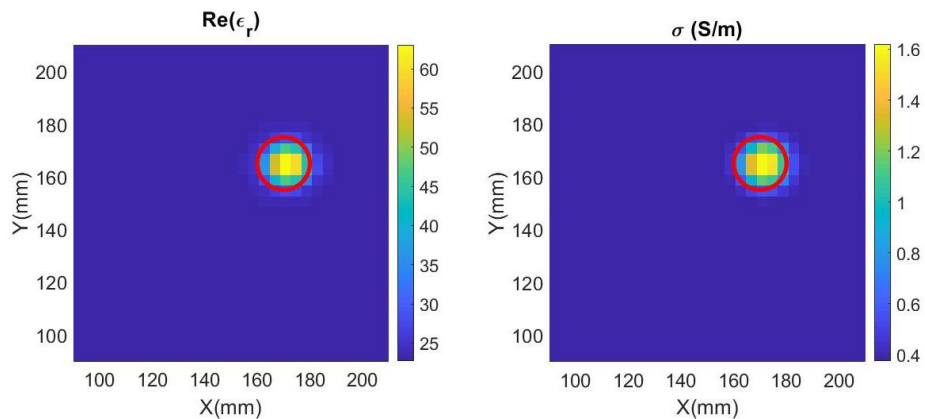


Figure 20: DBIM-TwIST reconstructions of electric properties. On left  $\epsilon_r$  distribution, on right  $\sigma$  distribution.

In Table 6 there are the expected values of  $\epsilon_r$  and  $\sigma$  and the values achieved in the last iteration.

Tissue	Expected	Results
Blood (1.1 GHz)	$\epsilon_r=63.06$ $\sigma=1.62$ S/m	$\epsilon_{r\_max}=63.08$ $\sigma_{max}=1.65$ S/m

Table 6: Comparison between expected and obtained electric properties values

In the graphs below there are the trend of Relative error (equation 18) and of Residual (equation 19).

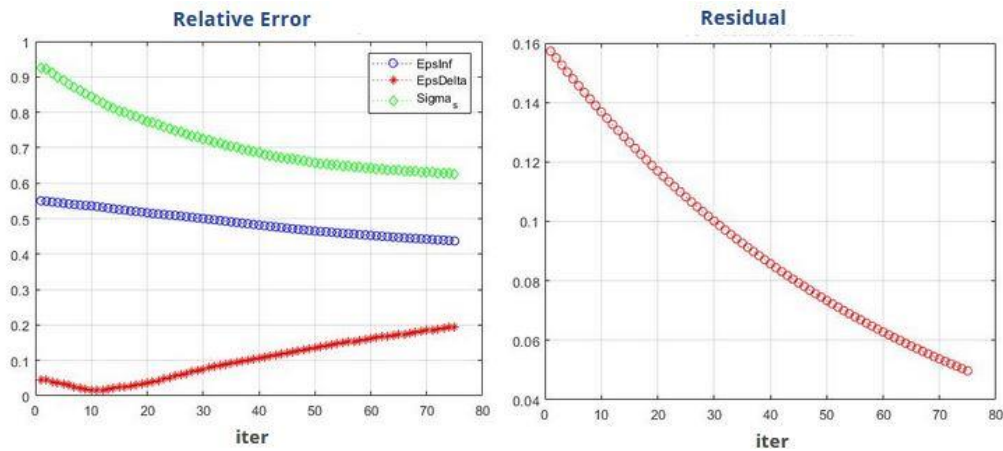


Figure 21: On left Relative error, on right Residual at each iteration

Once can notice that Debye parameters have a convergent trend towards a plateau. Instead, Residual has a strongly decreasing trend, but since it's not important to achieve great precision, 75 iterations is a good compromise between accuracy and computational time.

- CS

Algorithm settings:

- Work frequency: 1.1 GHz
- Number of iterations: 60
- Tetrahedrons size: 2 mm

In the Figure 22, there is the model created in Matlab.

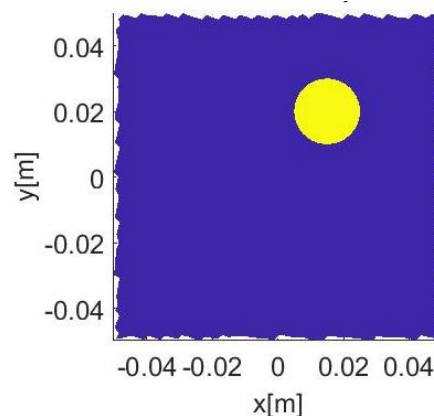
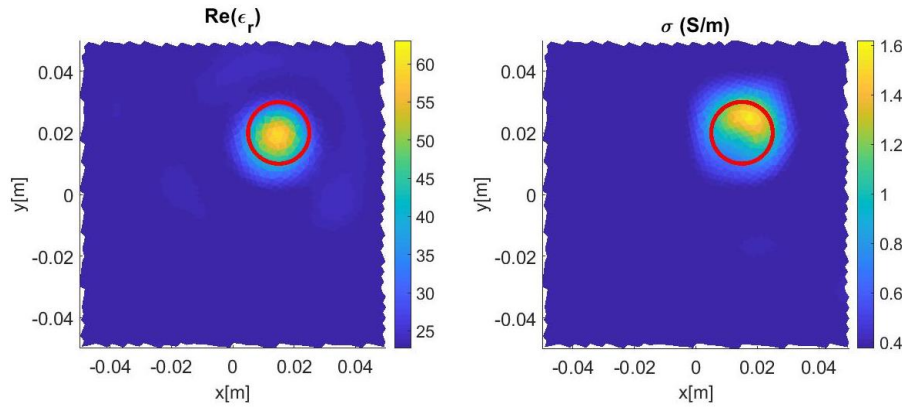


Figure 22: Matlab model, created with FEM of CS

Figure 23 shows reconstructions of electrical properties  $\epsilon_r$  and  $\sigma$ . The shape of the target is not exactly corresponding to the expected one, however the higher values of the two variables are contained in the red border that defines the target. An intermediate halo defines the passage from the values of the background and those of the target.



**Figure 23:** CS reconstructions of electric properties. On left  $\epsilon_r$  distribution, on right  $\sigma$  distribution.

Tissue	Expected	Results
Blood (1.1 GHz)	$\epsilon_r=63.06$ $\sigma=1.62$ S/m	$\epsilon_{r,max}=59.84$ $\sigma_{max}=1.78$ S/m

**Table 7:** Comparison between expected and obtained electric properties values.

In Figure 24 is reported the cost functional (logarithmic scale), once can notice that it starts with an high value but, during iterations, decreases. The number of iterations was chosen in order to have an acceptable tradeoff between  $\epsilon_r$  and  $\sigma$  value.

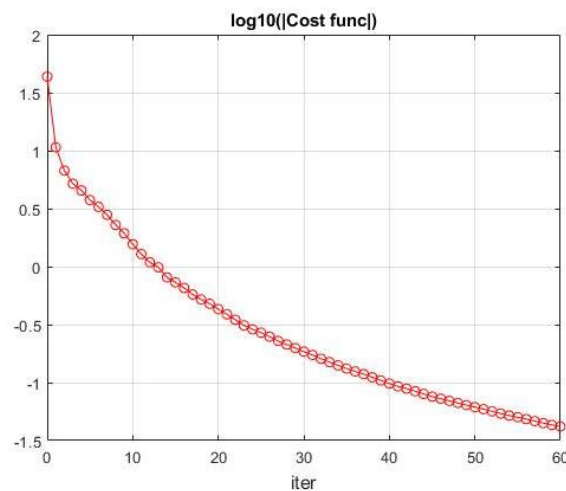


**Figure 24:** Cost functional at each iteration.

### 3.4.2 ALGORITHMS PERFORMANCE WITH SIMULATION DATA

For this section, the 3D model is created with an external software (it is the same for both the algorithms). In order to obtain the value of the calibrated field, a measurement without target (coupling medium only) and a measurement with the target are required. These 2 configurations are reported in Figure 25. Tetrahedrons dimensions are 1 mm in target and antennas, 2 mm in the domain region and 5 mm in the remaining space.

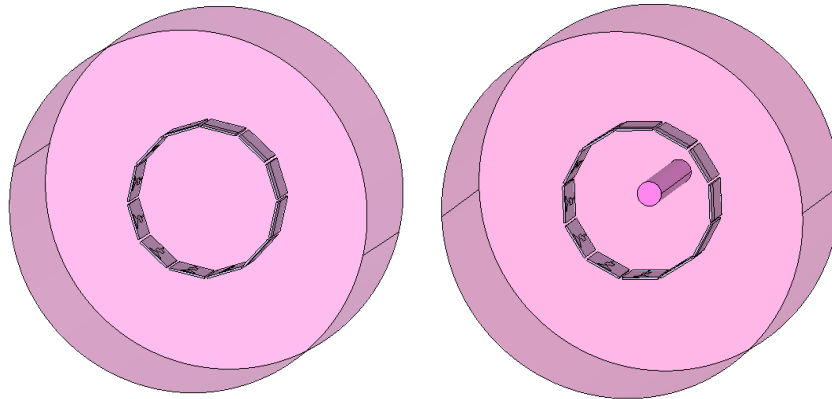


**Figure 25: Simulation model, created with a CAD software. On left model without blood target, on right model with blood target.**

In order to analyze how the electric field propagates in the domain of interest is used the software ParaView. Figure 26 shows distribution of the Electric field and its penetration through the blood target when only one antenna is on (the scale is in dB).

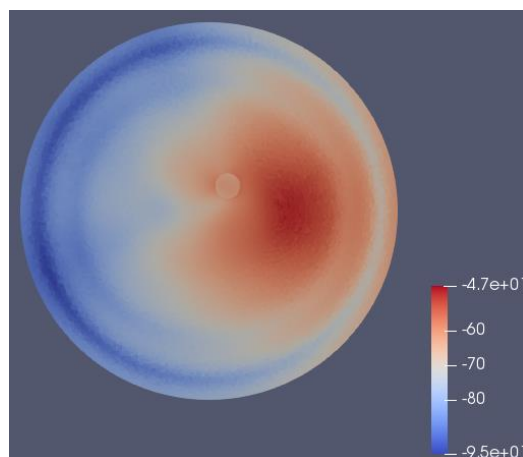


**Figure 26: Electric field distribution when only an antenna is on. The intensity scale on right is in dB.**

• *DBIM-TwIST*

Algorithm settings:

- Work frequency: 1.2 GHz
- Number of iterations: 100
- Resolution of the reconstructed image: 2 mm

In the Figure 27 there are the reconstructions of electrical properties  $\epsilon_r$  and  $\sigma$ . In this case the DBIM algorithm isn't able to reconstruct the correct distribution of the real part of  $\epsilon_r$ , in fact there is only a smeared shadow of the blood target. Regarding the  $\sigma$  reconstruction, the algorithm finds blood target position and shape, but the dimension is larger than the real one.

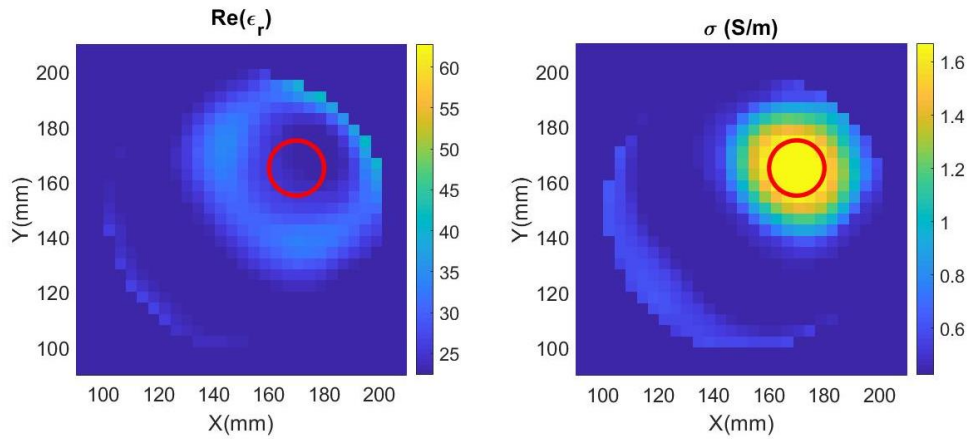


**Figure 27: DBIM-TwIST reconstructions of electric properties. On left  $\epsilon_r$  distribution, on right  $\sigma$  distribution.**

Also the values of the electric properties in the last iteration (Table 8) reflect the distribution behaviour:  $\epsilon_r$  fails increase, in fact even after 100 iterations it is very far from the real value; regarding  $\sigma$ , just as it exaggerates in size, it also exaggerates with value, however it isn't so far from the expected one.

Tissue	Expected	Results
Blood (1.2 GHz)	$\epsilon_r=62.81$ $\sigma=1.67$ S/m	$\epsilon_{r\_max}=41.56$ $\sigma_{max}=1.89$ S/m

**Table 8: Comparison between expected and obtained electric properties values.**

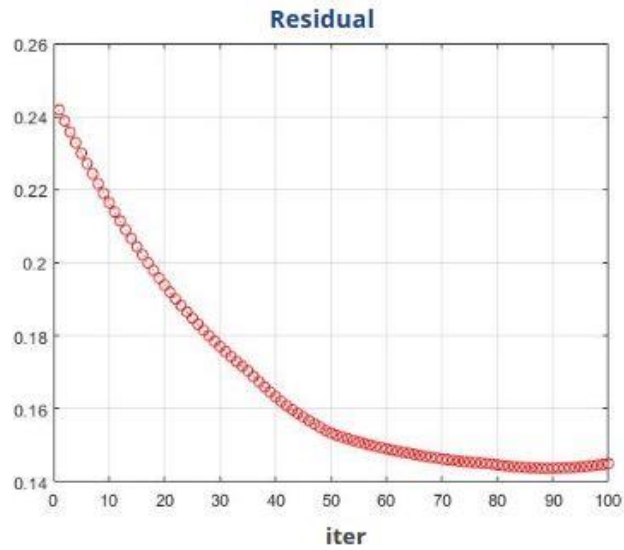


**Figure 28: Residual at each iteration.**

Also in this case, the residual hasn't particular trend, it decreases during the iterations.

In order to understand the causes of the strange reconstruction for  $\epsilon_r$ , an analysis of the input data trend is made. Below, there is the comparison between input data used for DBIM validation (red curve), simulation data without calibration (blue curve) and simulation data after calibration (green curve) as function of antennas index. In particular, in Figure 29 there is the module (dB) and in Figure 30 the phase (rad) for each radiating antenna and for a frequency equal to 1.2 GHz.

The green curves should overlap with the red ones, they have the same overall trend for both module and phase, but there are some distributed errors mostly in phase data.

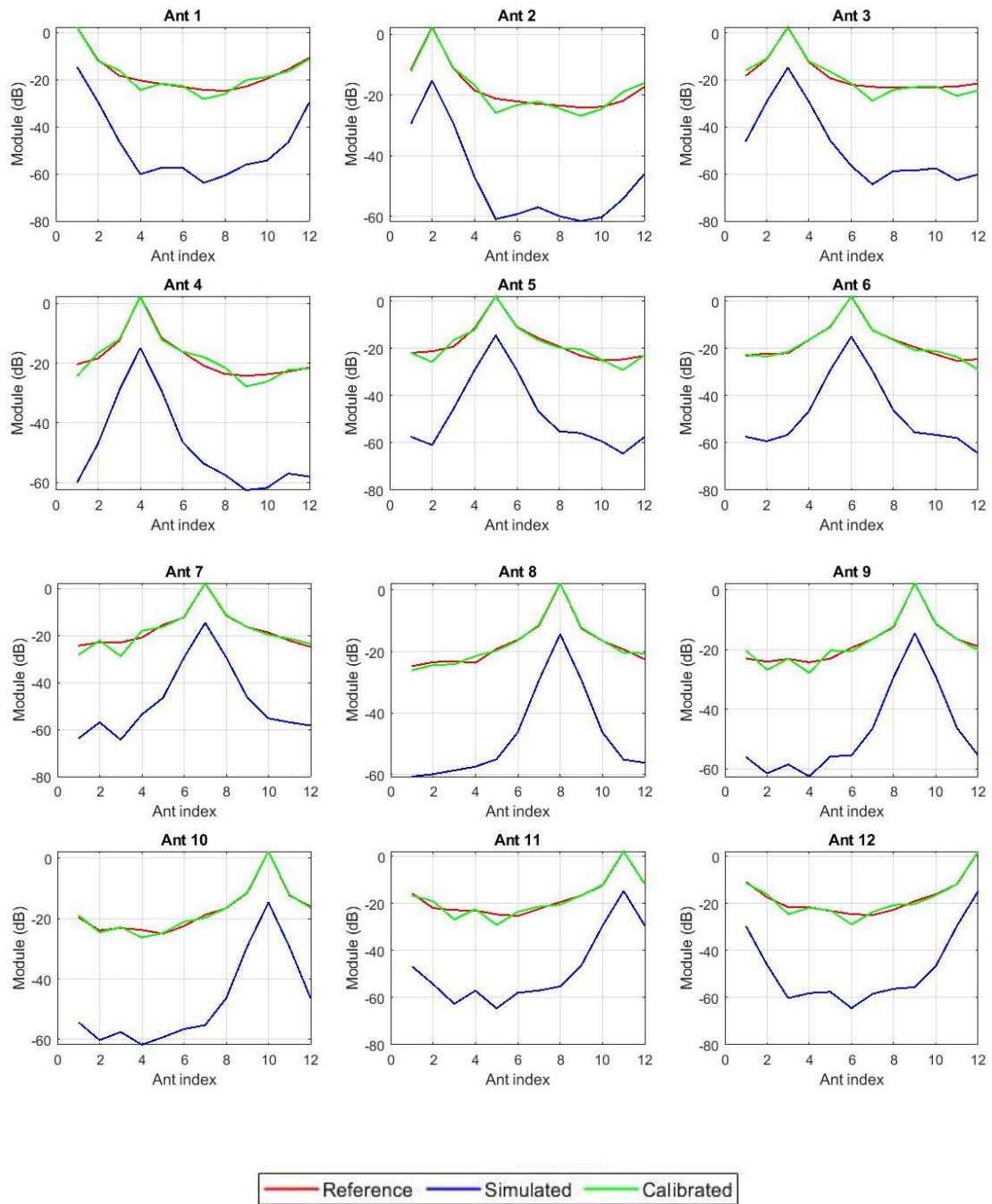


Figure 29: Module trend for each radiating antenna ( $f=1.2$  GHz)

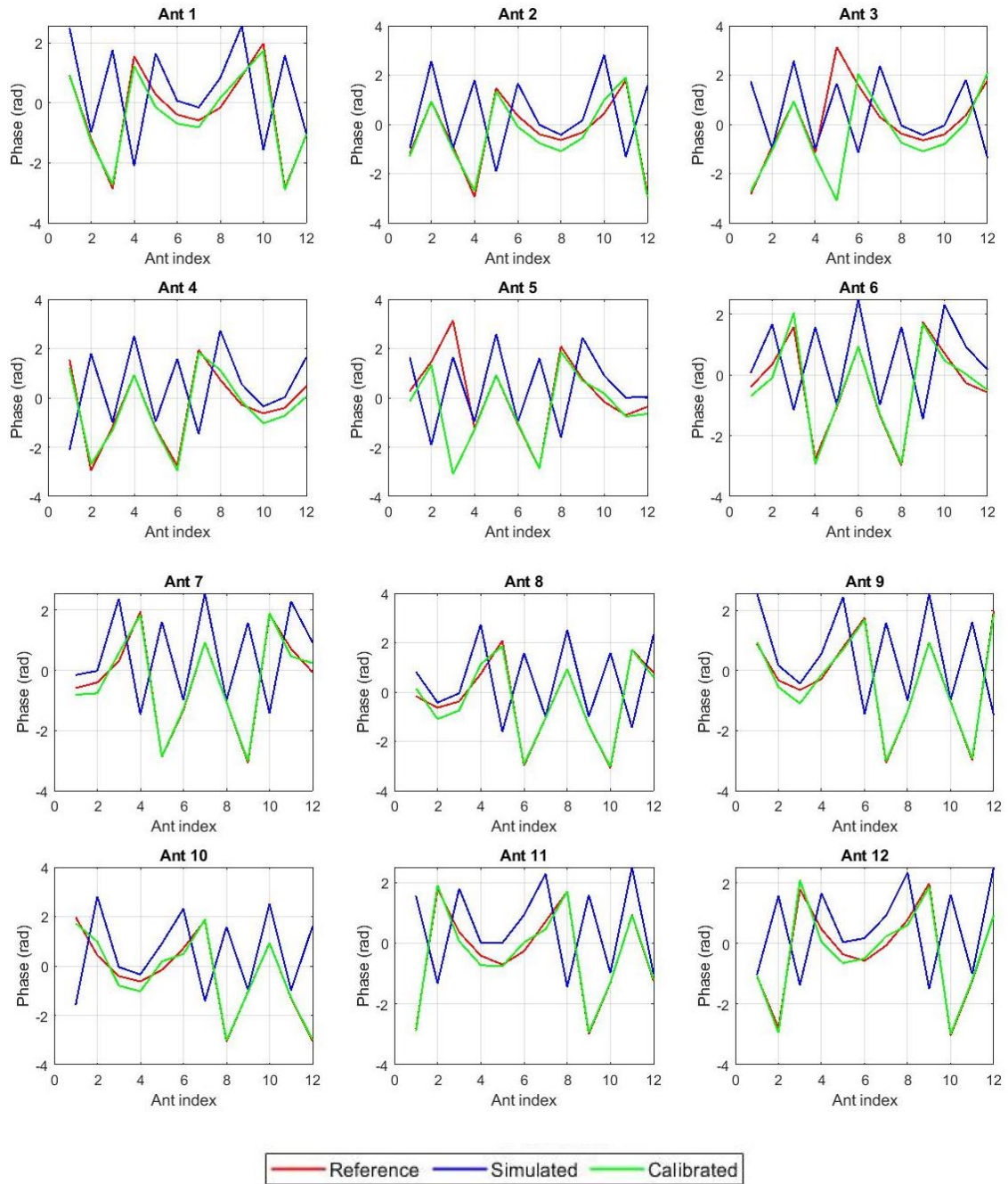


Figure 30: Phase trend for each radiating antenna ( $f=1.2$  GHz)

- CS

Algorithm settings:

- Work frequency: 1.2 GHz
- Number of iterations: 60
- Tetrahedrons size: 2 mm

Reconstructions of electrical properties  $\epsilon_r$  and  $\sigma$  are reported in Figure 31. In the distribution of the real part of  $\epsilon_r$ , after 60 iterations the algorithm finds the target but it is able to reconstruct a disk smaller than the expected one. Regarding the  $\sigma$  reconstruction, the algorithm finds blood target, but with a non-circular shape. In both the electrical properties, the center of reconstructed target is wrong, but very close to the real one.

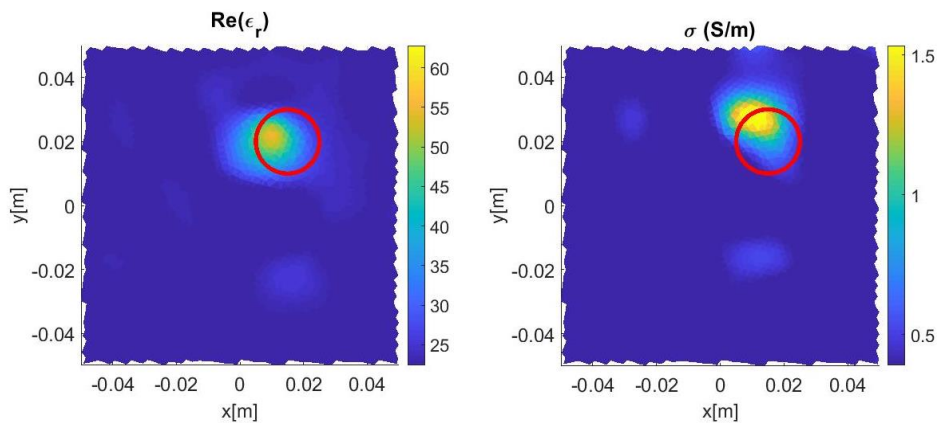


**Figure 31: CS reconstructions of electric properties. On left  $\epsilon_r$  distribution, on right  $\sigma$  distribution.**

In Table 9 once can notice that the algorithm wrong for both the electrical properties:  $\epsilon_r$  is too small and  $\sigma$  is too high.

Tissue	Expected	Results
Blood (1.2 GHz)	$\epsilon_r=62.81$ $\sigma=1.67$ S/m	$\epsilon_{r,max}=55.57$ $\sigma_{max}=2.08$ S/m

**Table 9: Comparison between expected and obtained electric properties values.**

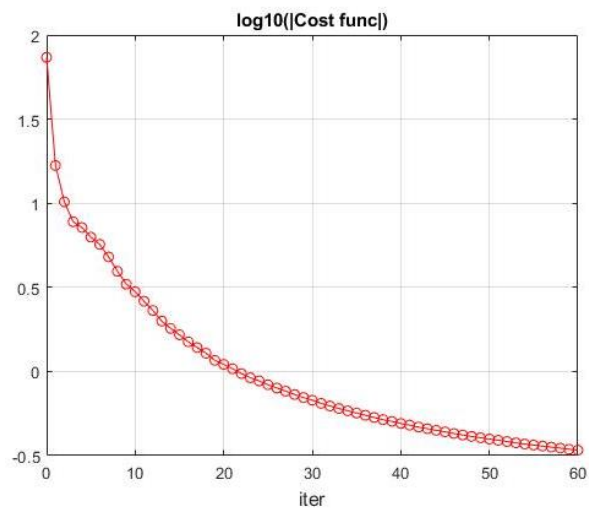


Figure 32: Cost functional at each iteration

### 3.5 MODEL 2

The second model, consists of a cylinder brain phantom immersed in a coupling medium and surrounded by twelve antennas. The brain phantom contains a cylinder blood phantom (as reported in Figure 33).

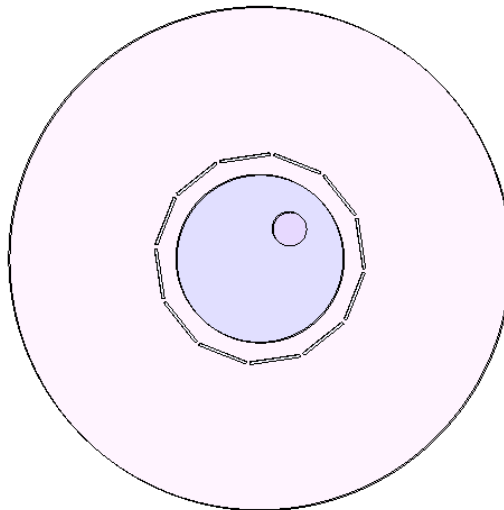


Figure 33: Geometry of model 2, realised with a CAD software

### 3.5.1 ALGORITHMS VALIDATION

In this section, there is the validation of the algorithms with model 2. The models are created in Matlab for both the algorithms, as for the model 1.

In the first part there is the validation of DBIM algorithm, with input model, reconstructed variables ( $\epsilon_r$  and  $\sigma$ ), relative error and residual. In the second part, there is the validation of CS algorithm, with input model, reconstructed variables ( $\epsilon_r$  and  $\sigma$ ) and cost functional.

- *DBIM-TwIST*

Algorithm settings:

- Work frequency: 1.1 GHz
- Number of iterations: 60
- Resolution of the reconstructed image: 2 mm

In the Figure 34, there is the model created in Matlab.

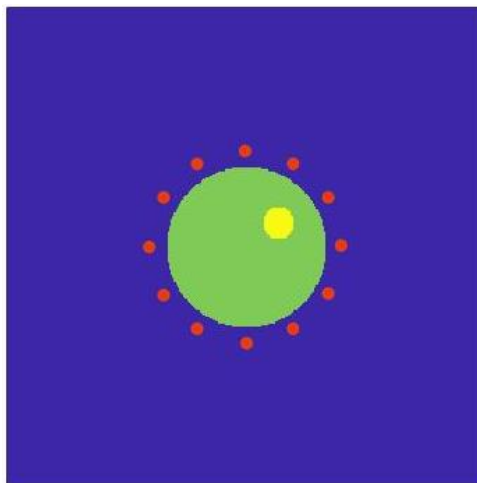


**Figure 34: Matlab model, created with Finite difference time domain method**

Figure 35 shows the reconstructions of the electric properties. As in the model 1, in this case the DBIM-TwIST algorithm works very well: the position and dimension of the target are right and also the variables values are very close to the expected ones.

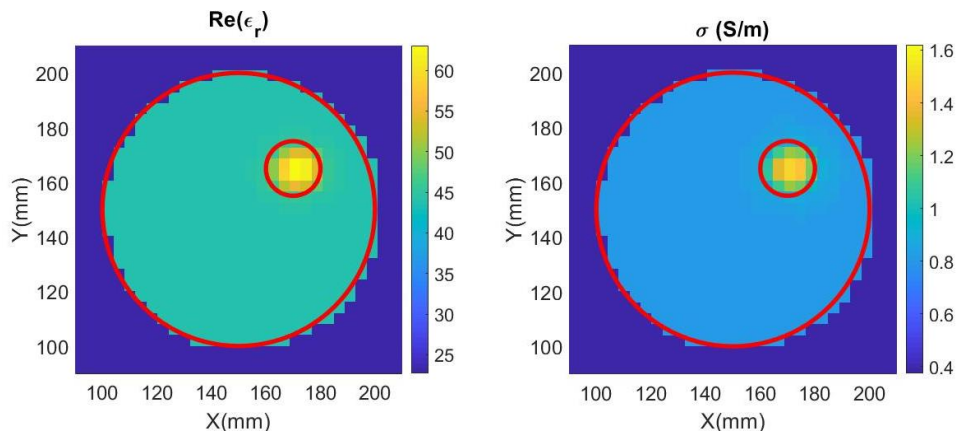


**Figure 35: DBIM-TwIST reconstructions of electric properties. On left  $\epsilon_r$  distribution, on right  $\sigma$  distribution.**

In Table 10 there are the expected values of  $\epsilon_r$  and  $\sigma$  and the values achieved in the last iteration.

Tissue	Expected	Results
Blood (1.1 GHz)	$\epsilon_r=63.06$ $\sigma=1.62$ S/m	$\epsilon_{r\_max}=63.08$ $\sigma_{max}=1.49$ S/m

**Table 10: Comparison between expected and obtained electrical properties values.**

In the graphs below there are the trend of the Relative error (equation 18) and of the Residual (equation 19).

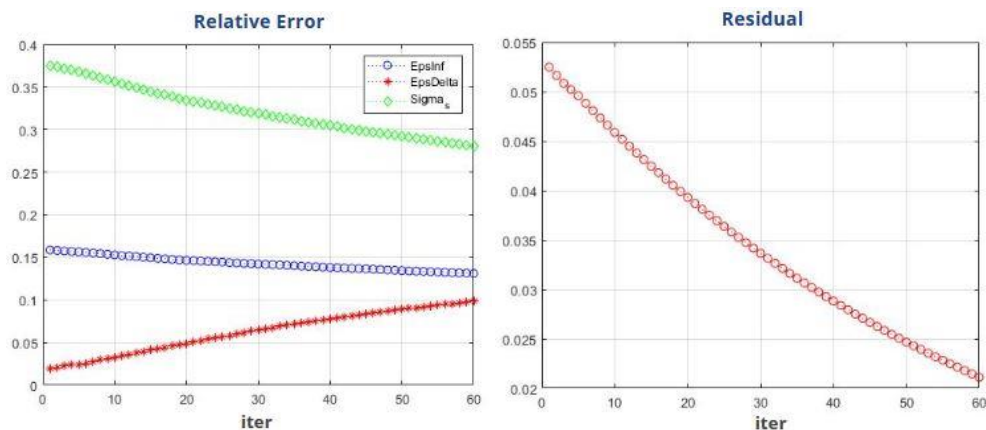


**Figure 36: On left Relative error, on right Residual at each iteration**

As for model 1, the Debye parameters have a convergent trend towards a plateau, instead, Residual has a strongly decreasing trend.

- CS

Algorithm settings:

- Work frequency: 1.1 GHz
- Number of iterations: 55
- Tetrahedrons size: 2 mm

In the Figure 37, there is the model for validation. The domain discretization in triangular elements is created with an external CAD software and after all the information about the mesh are used to create the model on Matlab.

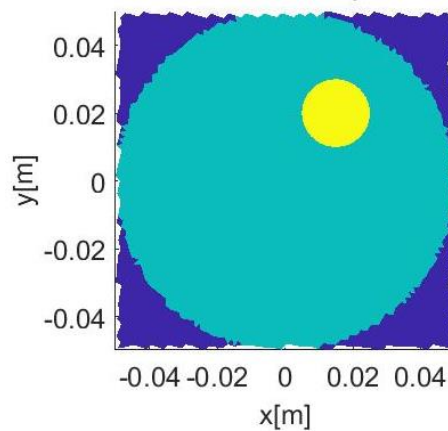


**Figure 37: Matlab model, created with FEM of CS**

Figure 38 shows the reconstructions of the electric properties. The algorithm seems to work better with this model than with the model 1, in fact with less iterations the reconstructed target is more similar to the expected one. Moreover, as reported in Table 11, the maximum values of the dielectric properties are almost equal to the real ones.

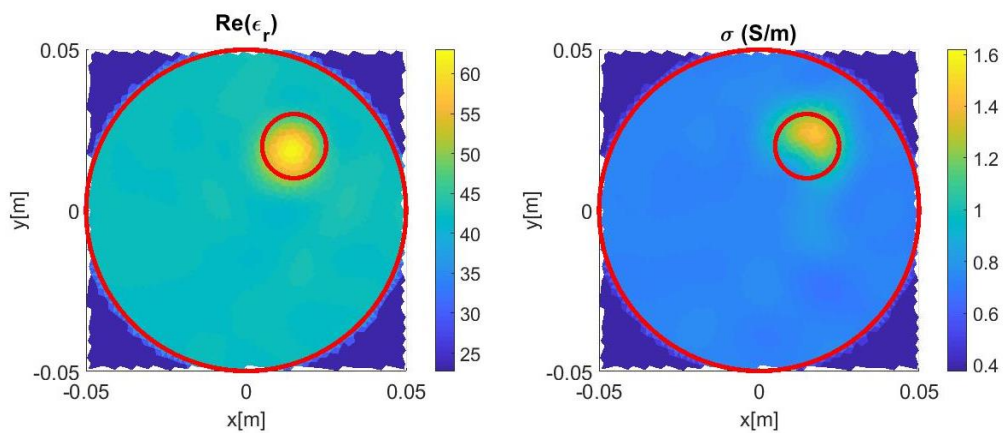


**Figure 38: CS reconstructions of electric properties. On left  $\epsilon_r$  distribution, on right  $\sigma$  distribution.**

Tissue	Expected	Results
Blood (1.1 GHz)	$\epsilon_r=63.06$ $\sigma=1.62$ S/m	$\epsilon_{r,max}=62.83$ $\sigma_{max}=1.62$ S/m

Table 11: Comparison between expected and obtained electrical properties values.

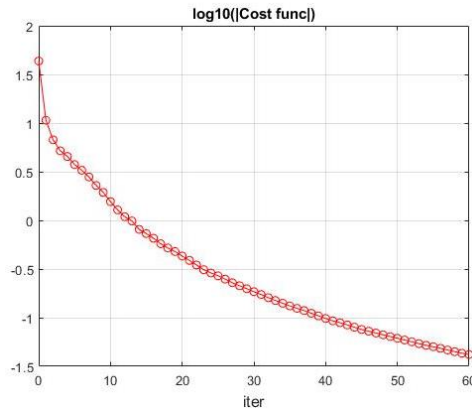


Figure 39: Cost functional at each iteration

### 3.5.2 ALGORITHMS SIMULATION

For this section, the 3D model is created with the external software. It is the same for both the algorithms. In order to obtain the value of the calibrated field, a measurement without target (coupling medium and brain phantom) and a measurement with the target are required. These 2 configuration are reported in Figure 40. Tetrahedrons dimensions are 1 mm in target and antennas, 2 mm in the domain region (brain phantom) and 5 mm in the remaining space.

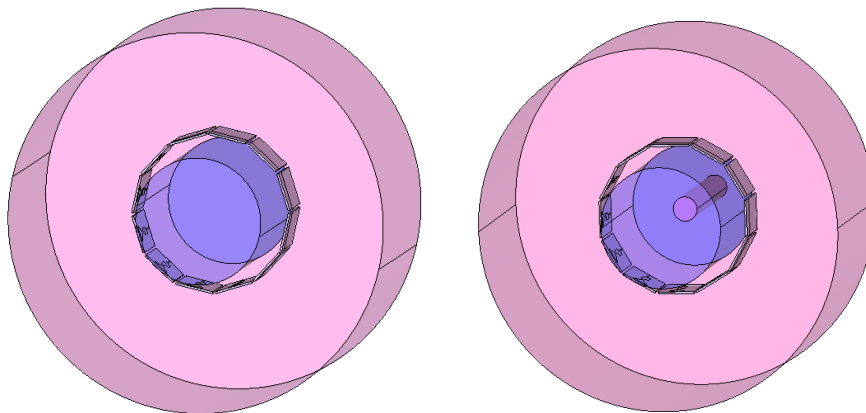


Figure 40: Simulation model, created with a CAD software. On left model without blood target, on right model with blood target.

As for the model 1, also here is reported the electric field distribution when only one antenna is on (the scale is in dB).

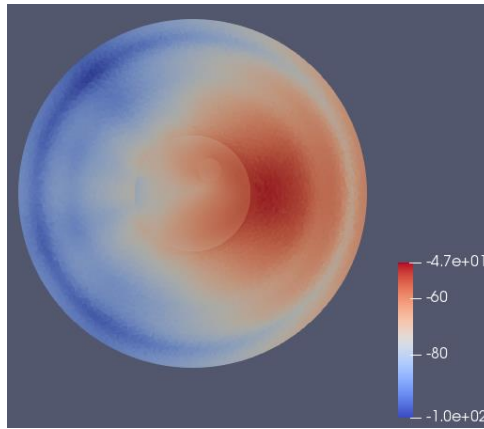


Figure 41: Electric field distribution when only an antenna is on. The intensity scale on right is in dB.

- *DBIM-TwIST*

Algorithm settings:

- Work frequency: 1.1 GHz
- Number of iterations: 150
- Resolution of the reconstructed image: 2 mm

Figure 42 shows DBIM-TwIST reconstruction. As for the model 1, the algorithm has more problems with the real part of  $\epsilon_r$ , in fact it feels the presence of target, but fails in the reconstruction (smeared shadow of the outline). Regarding  $\sigma$ , the algorithm finds the right position and draws target without holes, but with a size too large.

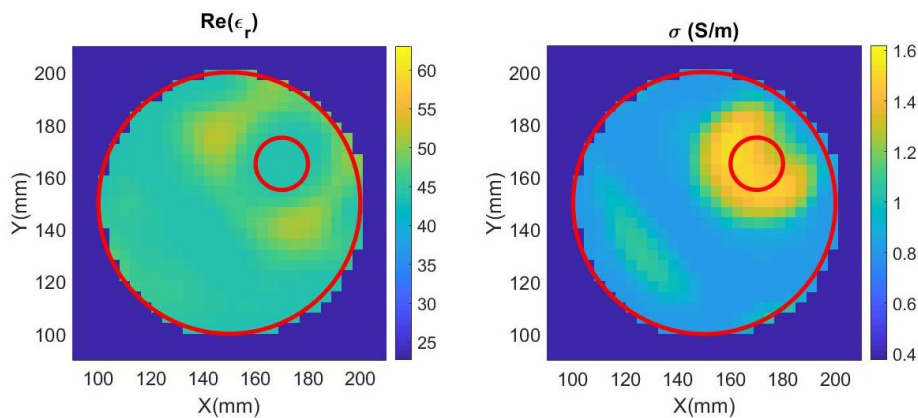


Figure 42: DBIM-TwIST reconstructions of electric properties. On left  $\epsilon_r$  distribution, on right  $\sigma$  distribution.

For what concern the maximum values of reconstructions, both  $\epsilon_r$  and  $\sigma$  are too small (Table 12).

Tissue	Expected	Results
Blood (1.1 GHz)	$\epsilon_r = 63.06$ $\sigma = 1.62 \text{ S/m}$	$\epsilon_{r\_max} = 52.21$ $\sigma_{max} = 1.52 \text{ S/m}$

Table 12: Comparison between expected and obtained electrical properties values.

The graphs in Figure 43 shows the residual error, it has a strange trend. In the last 50 iterations the residual error increases. This may be due to the wrong shape of the reconstructions, that moves measured values away from expected ones. In order to reach acceptable values of  $\epsilon_r$  and  $\sigma$ , a greater number of iterations was chosen.

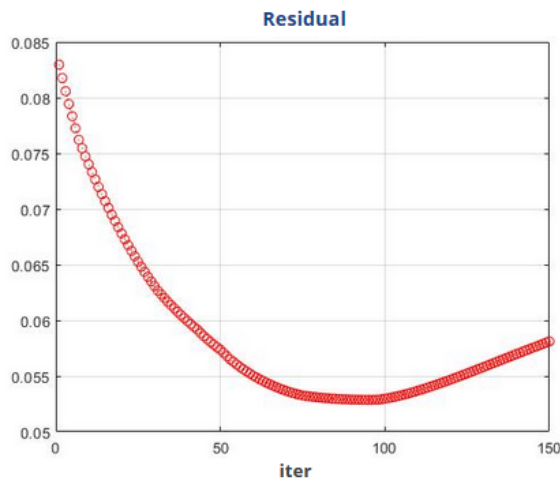
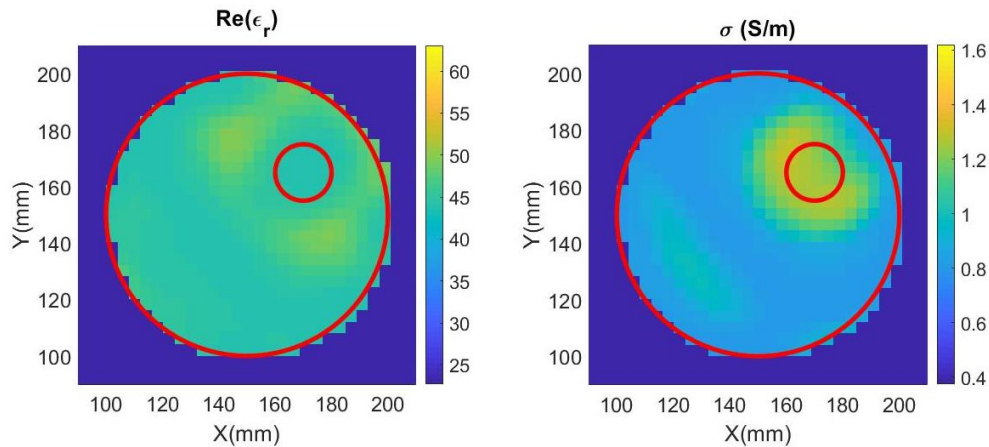


Figure 43: Residual at each iteration.

In Figure 44 are reported the dielectric properties distributions when the residual is minimum (75 iterations). It is already visible where the algorithm allocates the pixels with maximum values, but they are still too low ( $\epsilon_r = 49.52 \sigma = 1.30 \text{ S/m}$ ).



**Figure 44: DBIM-TwIST reconstructions of dielectric properties for the iteration with minimum residual. On left  $\epsilon_r$  distribution, on right  $\sigma$  distribution.**

As for the model 1, also for the model 2 an analyses of the input data trend is made. Below, there is the comparison between input data used for DBIM validation (red curve), simulation data without calibration (blue curve) and simulation data after calibration (green curve) as a function of antennas index. In particular, in Figure 45 there is the module (dB) and in Figure 46 the phase (rad) for each radiating antenna and for a frequency equal to 1.1 GHz. The green curves should overlap with the red ones, they have the same overall trend for both module and phase, but there are some small errors. However, it seems more precise than the model 1.

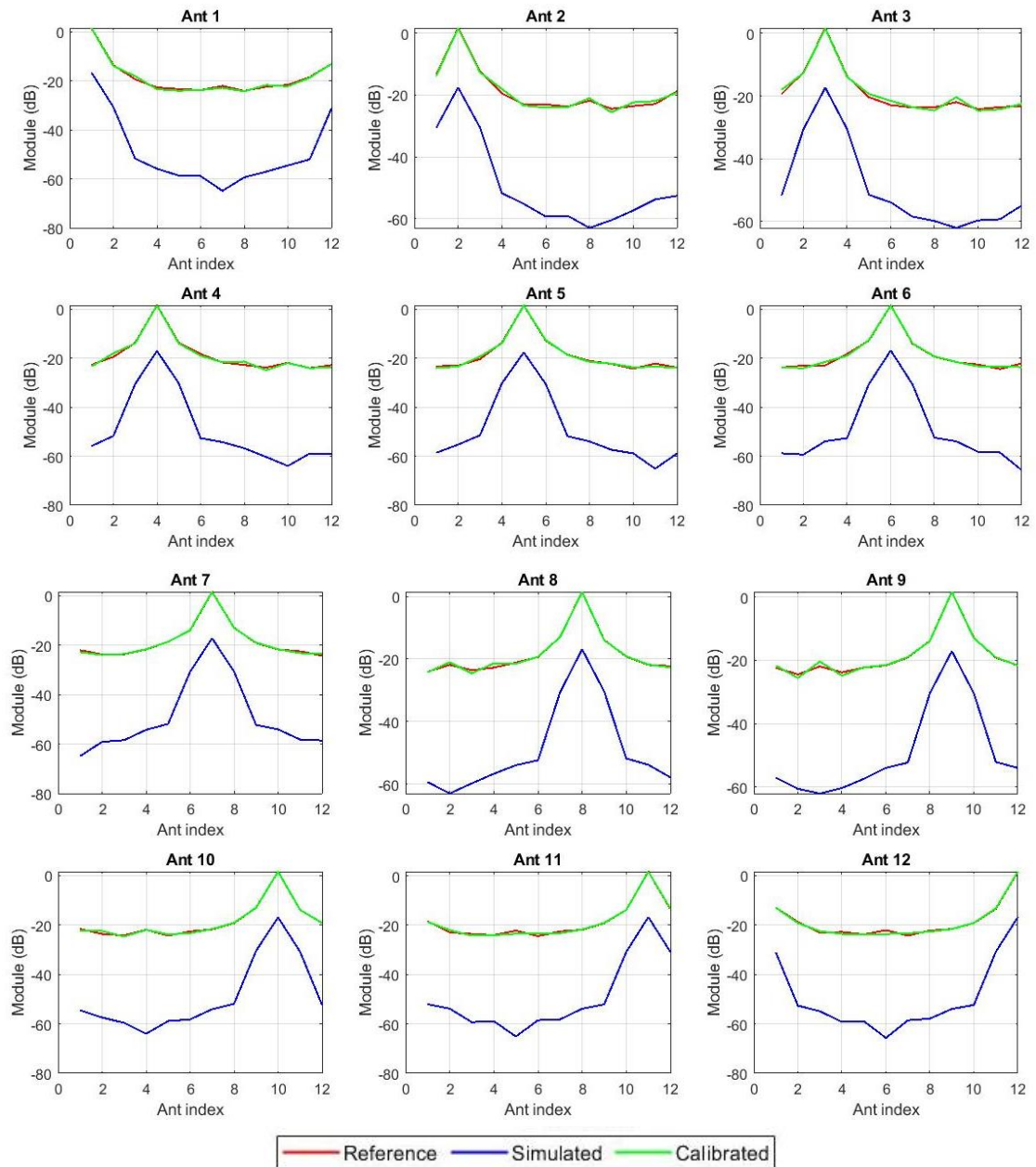


Figure 45: Module trend for each radiating antenna (  $f=1.1$  GHz)

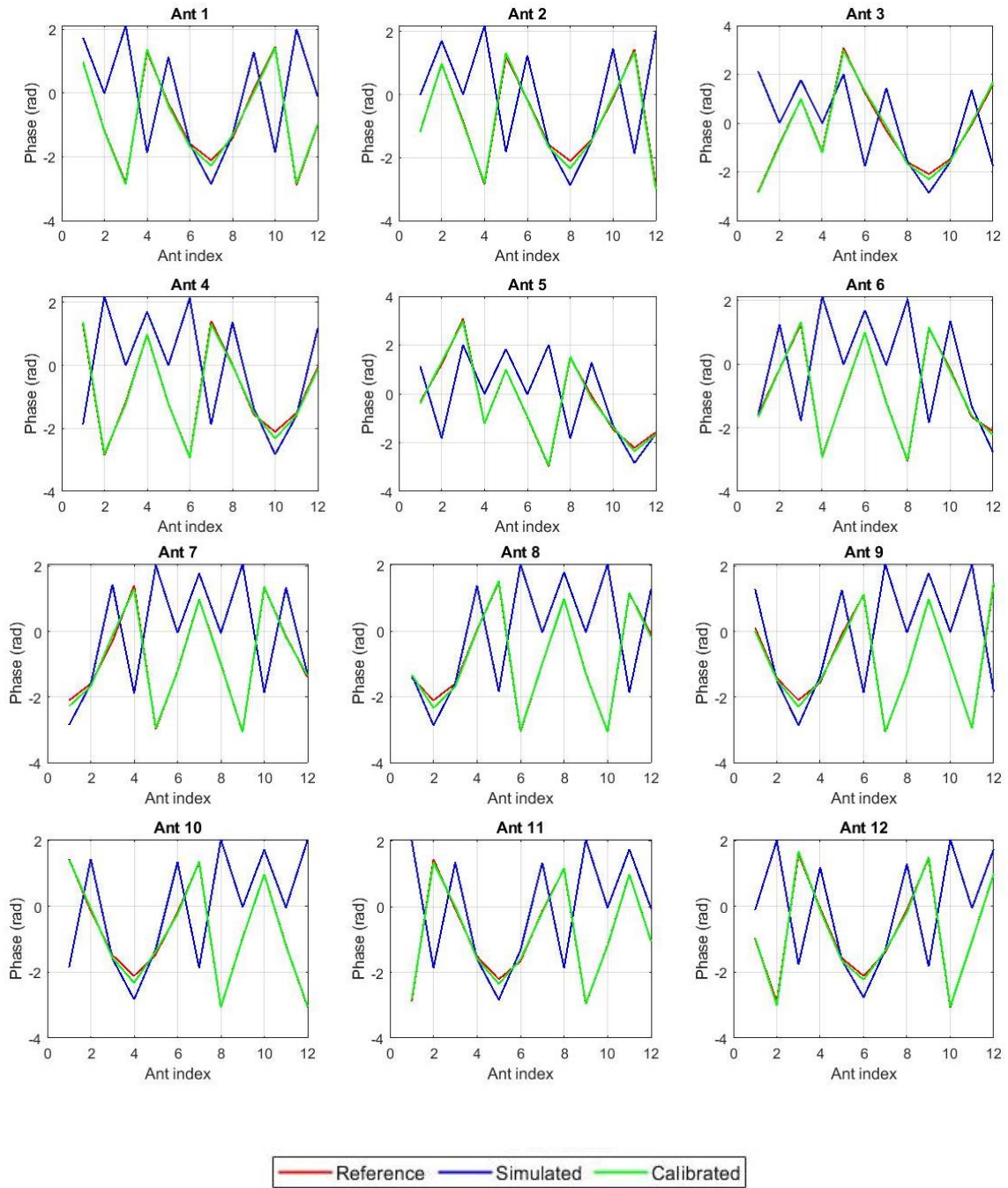


Figure 46: Phase trend for each radiating antenna ( $f=1.1$  GHz)

- CS

Algorithm settings:

- Work frequency: 1.1 GHz
- Number of iterations: 100
- Tetrahedrons size: 2 mm

In this case, CS finds almost the correct position of the target for both the dielectric properties. It requires a very high number of iterations, especially because conductivity reconstruction is slower to reach the correct value of blood target  $\sigma$ .

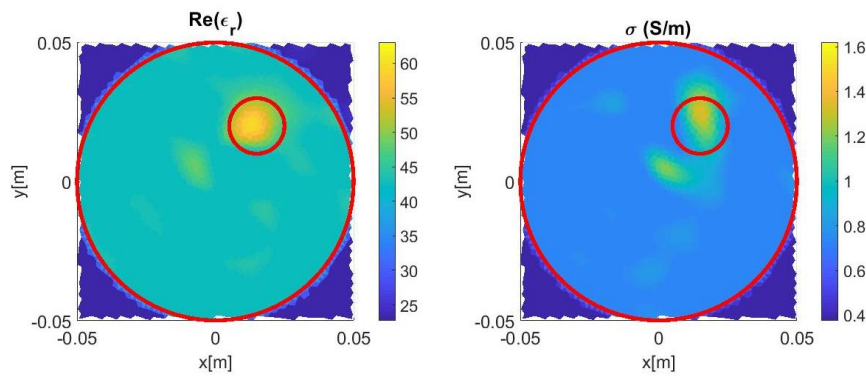


Figure 47: CS reconstructions of electric properties. On left  $\epsilon_r$  distribution, on right  $\sigma$  distribution.

Tissue	Expected	Results
Blood (1.1 GHz)	$\epsilon_r=63.06$ $\sigma=1.62$ S/m	$\epsilon_{r\_max}=60.07$ $\sigma_{max}=1.50$ S/m

Table 13: Comparison between expected and obtained electrical properties values.

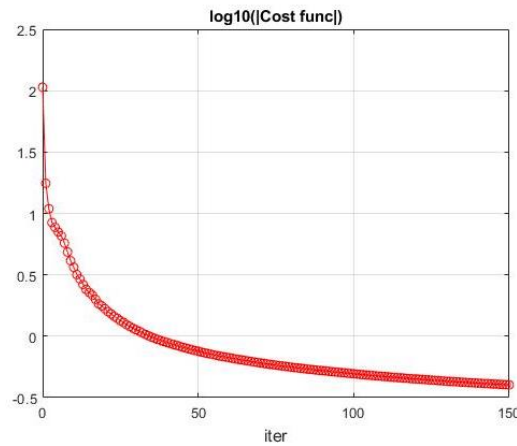


Figure 48: Cost functional at each iteration.

### 3.5.3 SUMMARY

In Validation section, both the algorithms work well, in fact they are able to reconstruct the correct position and dimension of blood target. Moreover, both the algorithms reach the exact dielectric properties values without difficulties.

In simulation section the DBIM has problems with  $\epsilon_r$  reconstruction, in fact it draws only a halo around the right position (for both models). However, the algorithm succeeds in  $\sigma$  reconstruction (position and shape of the target are exact). Due to the problem with  $\epsilon_r$  distribution, the two dielectric properties reach the exact values with different number of iterations.

CS performance are better than the DBIM (with simulation data): in model 1, with a few iteration CS finds the target for both the dielectric properties, even if the target position in the reconstructions are a bit different from the expected one; in model 2 the algorithm needs more iterations, but it find the correct position and for  $\epsilon_r$  also the exact target shape.

# 4. EXPERIMENTAL TESTING

## 4.1 MICROWAVE IMAGING SYSTEM

In this chapter, the input data of the two algorithms are measured data obtained in laboratory with a model similar to those used in the previous sections.

Figure 49 shows block diagram of the laboratory instrumentation used by the research group of Politecnico di Torino for the project MiBraScan [33].

There are five main blocks:

- Tank with the antennas;
- Switch matrix for directing transmitted and received radiofrequency signals;
- Vector Network Analyzer (VNA) for transmitting and receiving signals;
- Processing block for acquired data;
- Display to visualize the reconstructed image.

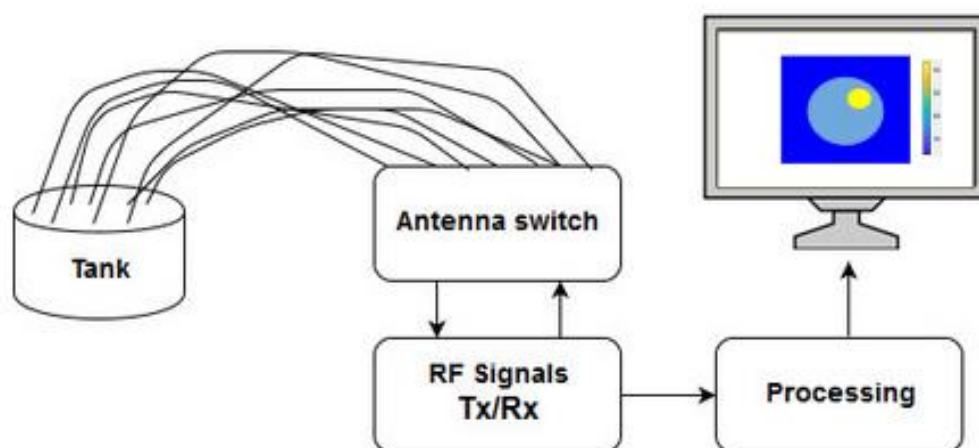


Figure 49: Instrumentation block diagram

Antennas are located on a circumference and they can operate as transmitters and receivers. Vector Network Analyzer (VNA) generates the signal and a switch matrix sends this signal to only one antenna and sets all the others as receivers.

The VNA has only 2 ports (one transmitting and one receiving), so the controller configures switch matrix to link simultaneously only one transmitter and one receiver. The VNA obtains scattering parameters from the ratio between received and sent signal. The system makes the acquisition for each antenna that acts as transmitter, so for each of  $N$  antennas it recovers  $N$  values (also the transmitter is used as receiver).

The acquisition block output is a file containing the matrix  $N \times N$  with scattering parameters. This file is the input of the processing block, in which there is the image reconstruction algorithm. Finally, display shows the reconstruction image [17].

Obviously, in this case there are more complications than in simulations: one of the most important problem is noise, which causes data variability.

Moreover, the approximations used in the algorithms (respected mostly in validation models) turn away image reconstruction from reality.

Figure 50 shows equipment used to make measurements, instead in Figure 51 there is tank filled with the coupling liquid and with the phantom surrounded by twelve antennas.



Figure 50: Realized microwave imaging system [7].



Figure 51: Tank filled with the coupling liquid with phantom and RX/TX antennas inside [7].

Figure 52 shows 3D-printed phantoms designed to model a brain with stroke. Phantom, in Figure 42a and 42b, models the brain. It is a cylindrical cavity made of acrylonitrile butadienestyrene (ABS) with a diameter of 10 cm and a height of 16 cm and the cap has three holes for smaller ABS cylinders (Figure 42c) insertion. The larger hole is a 1.8-cm-diameter, instead the other two are 1.4-cm-diameter. Antennas and phantom external surface have a relative distance of 3 cm.

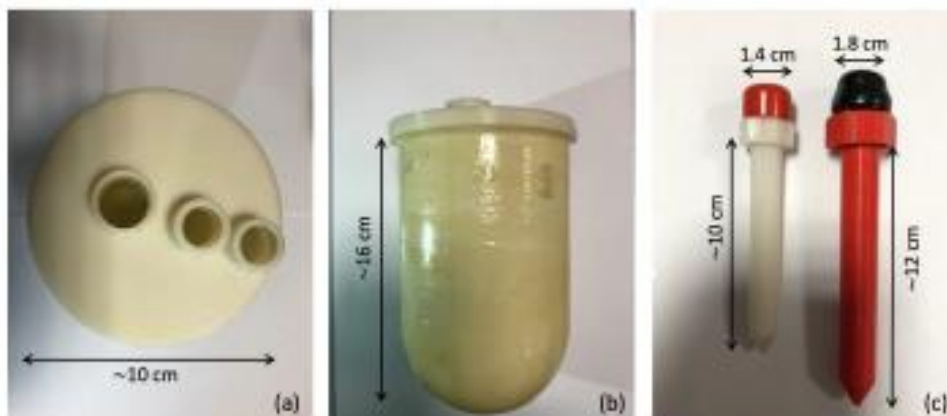


Figure 52: Phantom; (a) top view, (b) side view, (c) inserted cylinders [7].

## 4.2 MEASUREMENTS PROCESSING

Before giving the input data to the algorithms, there is a processing divided into at most four steps.

The first step is a de-embedding operation, that allows to shift the reference planes directly at the antennas port. VNA provides the scattering matrix of the whole system: paths and device under test (DUT).

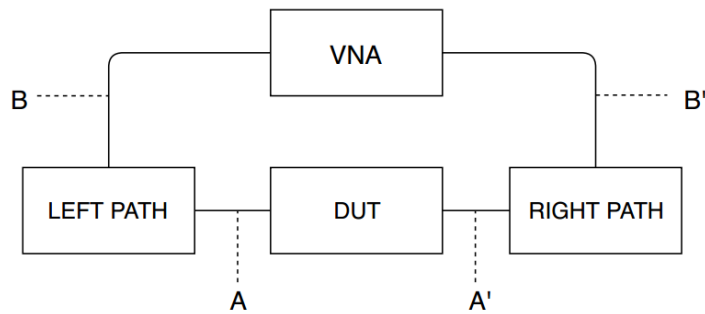


Figure 53: Measures with the VNA

Figure 53 shows a simplify scheme of VNA measures. In the “PATH LEFT” there is the signal which transits from the port to the antenna by the cables and the switcher, instead the signal which transits from the second antenna to the second port by the cables and the switcher, travels in the “PATH RIGHT”. Hence, the DUT is constituted of the antennas and phantom. VNA measures the path between B and B’. Different path are measured in order to obtain the transmission matrix (and then the S matrix) of DUT (A - A’) with the operation described in Figure 54:

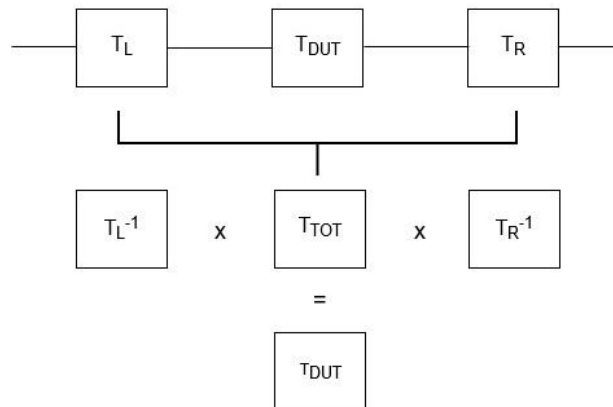


Figure 54: De-embedding operation on the Scattering matrix

After that, there is Time Gating (TG) applied in order to reduce multiple reflections within the tank. The VNA has the feature called “gating” that removes transmission and reflection responses. The gate is applied in time domain and, after that, data can be converted back in frequency domain [34].

The third fundamental step, before the image reconstruction, is calibration. It has the same form used for simulation model (equal for two algorithms) [31], [32]:

$$|E_{with\ target}^{calibrated}|_{dB} = |S_{with\ target}^{meas}|_{dB} - |S_{not\ target}^{meas}|_{dB} + |E_{not\ target}^{ref}|_{dB} \quad (64)$$

$$Pha(E_{with\ target}^{calibrated}) = Pha(S_{with\ target}^{meas}) - Pha(S_{not\ target}^{meas}) + Pha(E_{not\ target}^{ref}) \quad (65)$$

With:

- $Pha$  operator extrapolates the phase of his argument;
- $E_{with\ target}^{calibrated}$ , reflected field when object of interest is in reconstruction area;
- $S_{with\ target}^{meas/sim}$ , measured data when object of interest is in reconstruction area;
- $S_{not\ target}^{meas/sim}$ , measured data when object of interest isn't in reconstruction area;
- $E_{not\ target}^{ref}$ , incident field (no object in reconstruction area). It is calculated in the algorithms (DBIM and CS).

Finally, for each radiating antenna, the contribute of neighbouring antennas has been eliminated because they have a strong coupling with the radiating one. This last step removes information, but at the same time removes noisy data and speed up the convergence.

### 4.3 EXPERIMENTAL RESULTS

According to the phantom structure, three cases are considering. Inner cylinders, that plays haemorrhagic stroke role, can be inserted in the phantom, mimicking the brain.

- **Case 1:** cylinder with 1.8 cm diameter, centered at (-13 7.5) cm (near the center of the phantom);

- **Case 2:** cylinder with 1.4 cm diameter, centered at (-13 -7.5) cm (near the center of the phantom);
- **Case 3:** cylinder with 1.4 cm diameter, centered at (26.5 -26.5) cm (close to the periphery of the phantom).

The geometry of the three models are reported in Figure 55.

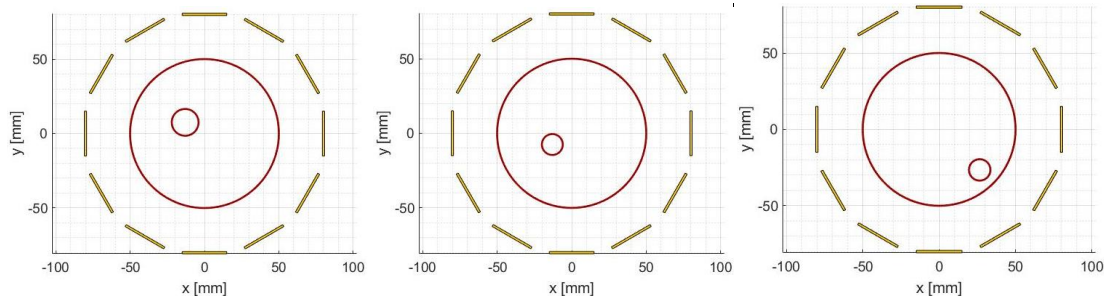


**Figure 55:** the three geometries used for algorithms comparison when the input are measured data. In each model there is blood phantom immersed in the coupling medium. From left to right, there are case 1, case 2 and case 3.

Also, for the measured data, the best frequency is chosen for each case in the range 1 GHz-1.5 GHz, with a step of 0.1 GHz.

For the case 1, the complete analysis is reported, instead for case 2 and 3 only the best condition is shown.

#### 4.3.1 Case 1

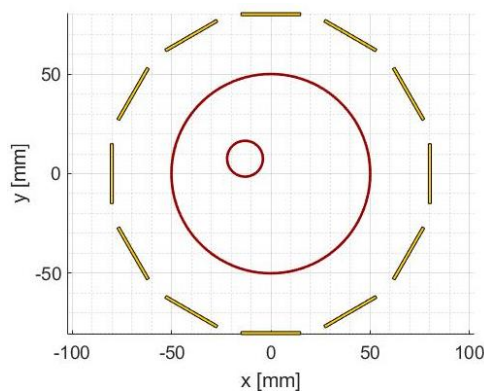


**Figure 56:** Geometry in case 1.

• *DBIM-TwIST*

In Figure 57 are reported the results obtained with four different input data, from the first column on the left to the last on the right: raw data, raw data with de-embedding, raw data with TG, raw data with de-embedding and TG. In all these case, input data are calibrated and contribute of neighbouring antennas has been eliminated. They are obtained with a frequency equal to 1 GHz and each of input data are elaborated with the number of iterations that performs better.

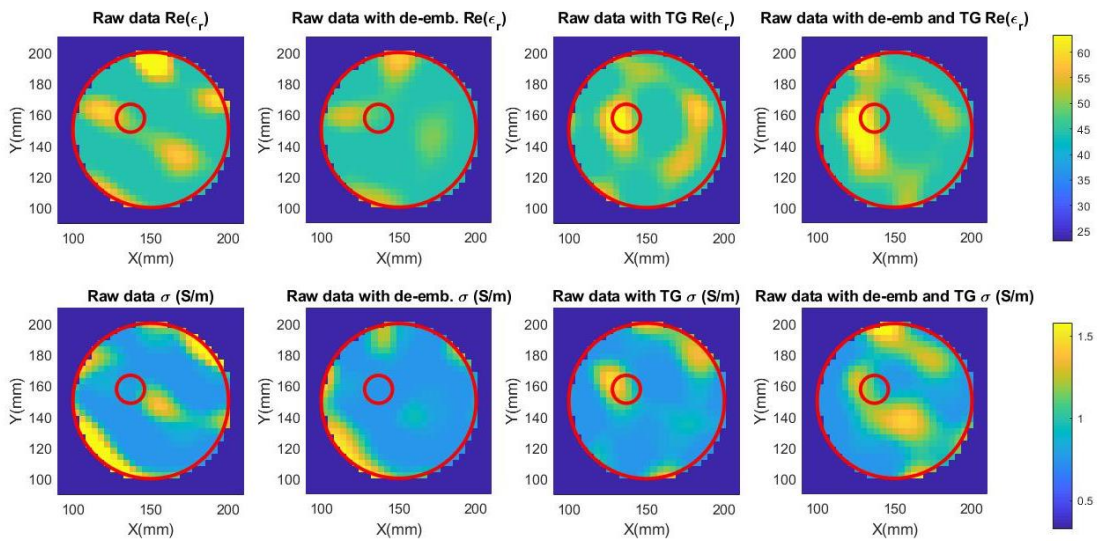


**Figure 57: DBIM-TwIST results in case 1, with a frequency equal to 1 GHz. First column: raw data (25 iterations), second column: raw data with de-embedding (35 iterations), third column: raw data with Time Gating (50 iterations), fourth column: raw data with de-embedding and TG (25 iterations). First row:  $\epsilon_r$ , second row:  $\sigma$ .**

Results obtained with raw data, recognizes the blood target presence but locates it in wrong and scattered positions. De-embedding can delete target reconstructed in wrong positions, but at the same time, it cancels some important information. For this reason, input data processed with TG are more precise than input data processed with de-embedding and TG.

Below, the best results (raw data with TG) are treated more specifically.

Algorithm settings in the case raw data with TG:

- Work frequency: 1.0 GHz
- Number of iterations: 50

- Resolution of the reconstructed image: 2 mm

DBIM algorithm can feel the presence of the blood target and reconstructs it quite well. Reconstructions strongly depend from the working frequency. Electrical properties values are very close to the expected ones, as reported in Table 14.

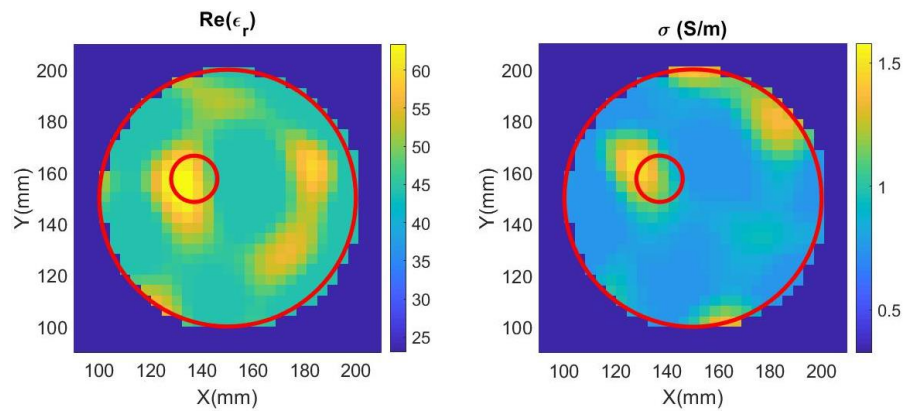


Figure 58: DBIM-TwIST reconstructions of electric properties without the contributions of neighbouring antennas. Input data: raw data with TG. On left  $\epsilon_r$  distribution, on right  $\sigma$  distribution.

Tissue	Expected	Results
Blood (1.0 GHz)	$\epsilon_r=63.41$ $\sigma=1.58$ S/m	$\epsilon_{r\_max}=65.50$ $\sigma_{max}=1.48$ S/m

Table 14: Comparison between expected and obtained electrical properties values.

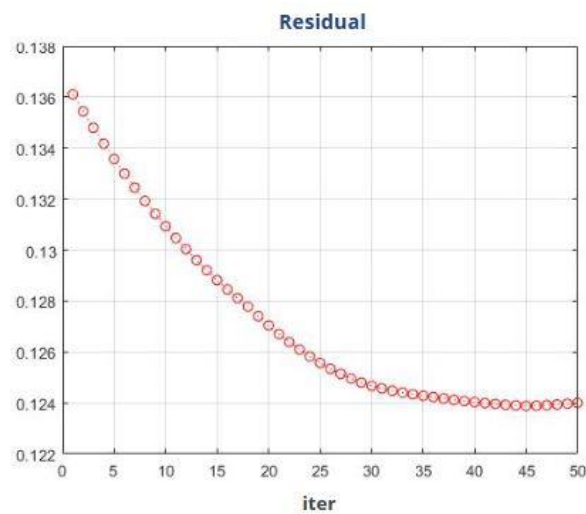
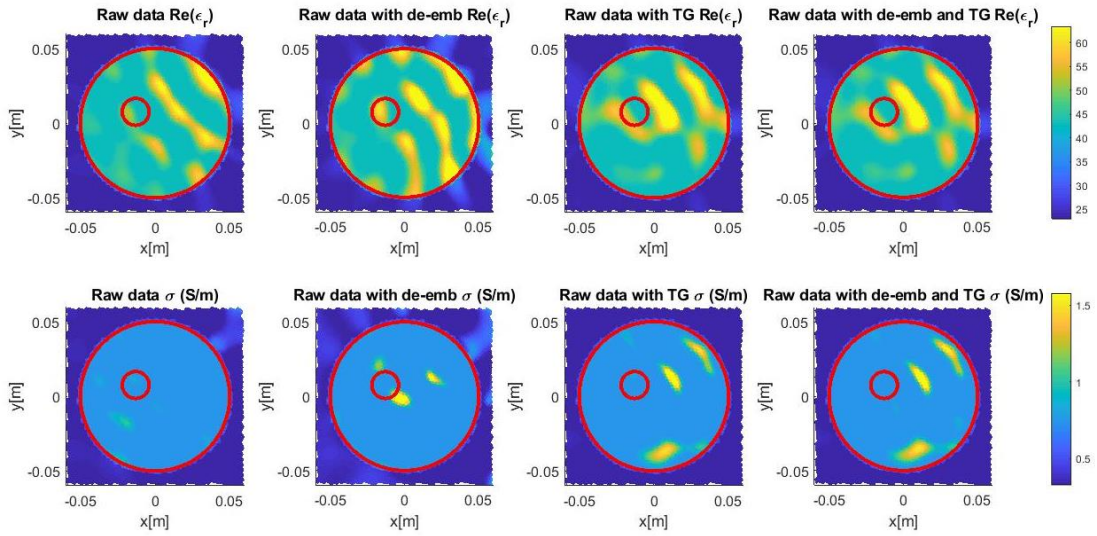


Figure 59: Residual at each iteration

- CS

Also, for CS are reported the results obtained with four different input data (Figure 60), from the first column on the left to the last on the right: raw data, raw data with de-embedding, raw data with TG, raw data with de-embedding and TG. In all these case, input data are calibrated and contribute of neighbouring antennas has been eliminated. They are obtained with a frequency equal to 1 GHz and a number of iterations equal to 10.



**Figure 60: CS results in case 1, with a frequency equal to 1 GHz. First column: raw data (10 iterations), second column: raw data with de-embedding (10 iterations), third column: raw data with Time Gating (10 iterations), fourth column: raw data with de-embedding and Time Gating (10 iterations). First row:  $\epsilon_r$ , second row:  $\sigma$ .**

In CS, the results appear worse than in DBIM-TwIST with all type of input data. However, the better reconstructions are with raw data with TG and with raw data with de-embedding and TG, because blood target reconstructions are less scattered than for the other ones (raw data and raw data with de-embedding). In order to minimise the overall computational cost and the processing, raw data with TG are chosen.

The best case (raw data with TG) is treated more specifically.

Algorithm settings in the case raw data with TG :

- Work frequency: 1.0 GHz
- Number of iterations: 10
- Tetrahedrons size: 2 mm

As shown in Figure 61, CS feels the presence of blood target, but it has some problems in reconstructions: target position and shape are wrong. However, for  $\epsilon_r$  more intense yellow halo, is very close to the right position of the target.

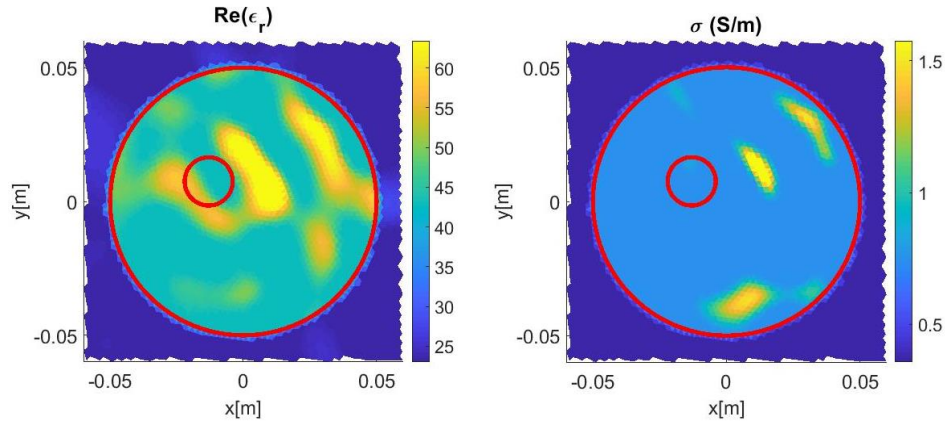


**Figure 61: CS reconstructions of electric properties without the contributions of neighbouring antennas. Input data: raw data with TG. On left  $\epsilon_r$  distribution, on right  $\sigma$  distribution.**

Moreover, the algorithm reaches very high values even after 10 iterations and it diverges very quickly.

Tissue	Expected	Results
Blood (1.0 GHz)	$\epsilon_r=63.41$ $\sigma=1.58$ S/m	$\epsilon_{r\_max}=76.33$ $\sigma_{max}=2.18$ S/m

**Table 14: Comparison between expected and obtained electrical properties values.**

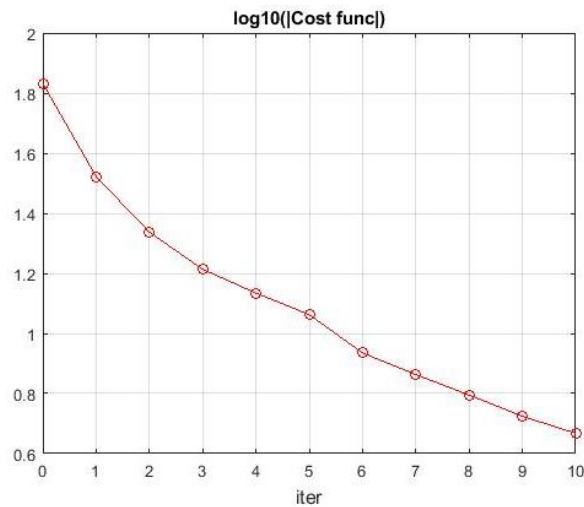


**Figure 62: Cost functional at each iteration**

### 4.3.2 Case 2

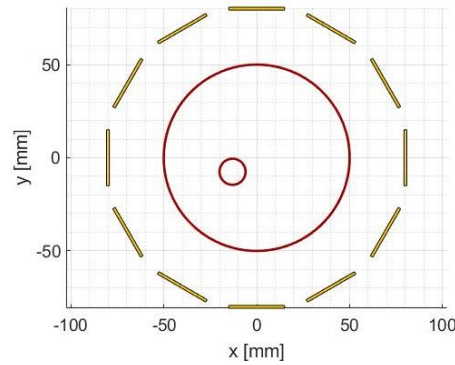


Figure 63: Geometry in case 2.

- *DBIM-TwIST*

Algorithm settings in the case raw data, with TG without the contributions of neighbouring antennas and with calibration:

- Work frequency: 1.0 GHz
- Number of iterations: 15
- Resolution of the reconstructed image: 2 mm

Figure 64 shows DBIM-TwIST reconstructions. The algorithm feels the presence of blood target that is reconstructed in positions not so far from the real one, mostly for  $\epsilon_r$ . Target dimension is very small and probably this is the reason of the difficulty in shape and size reconstruction.

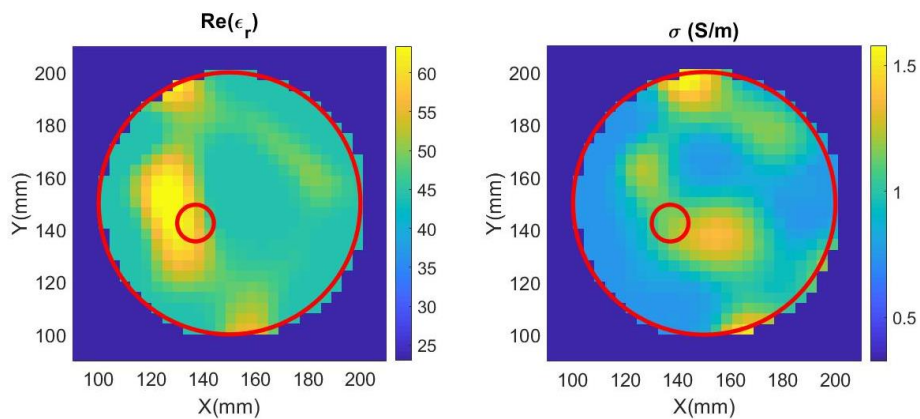


Figure 64: DBIM-TwIST reconstructions of electric properties without the contributions of neighbouring antennas. Input data: raw data with TG. On left  $\epsilon_r$  distribution, on right  $\sigma$  distribution.

In Table 15 are reported expected and obtained values of dielectric properties. They are very close, but increasing the number of iterations the error in  $\epsilon_r$  and  $\sigma$  raises.

Tissue	Expected	Results
Blood (1.0 GHz)	$\epsilon_r=63.41$ $\sigma=1.58$ S/m	$\epsilon_{r\_max}=66.25$ $\sigma_{max}=1.70$ S/m

Table 15: Comparison between expected and obtained electrical properties values.

In Figure 65 is reported the reconstructions of the same model but after 25 iterations. Once can notice that after 15 iterations the algorithm obtains the optimal solution, instead with the increase of iterations the reconstruction moves away from the exact model and dielectric properties continue to increase (Table 16). It implies an instability in convergence.

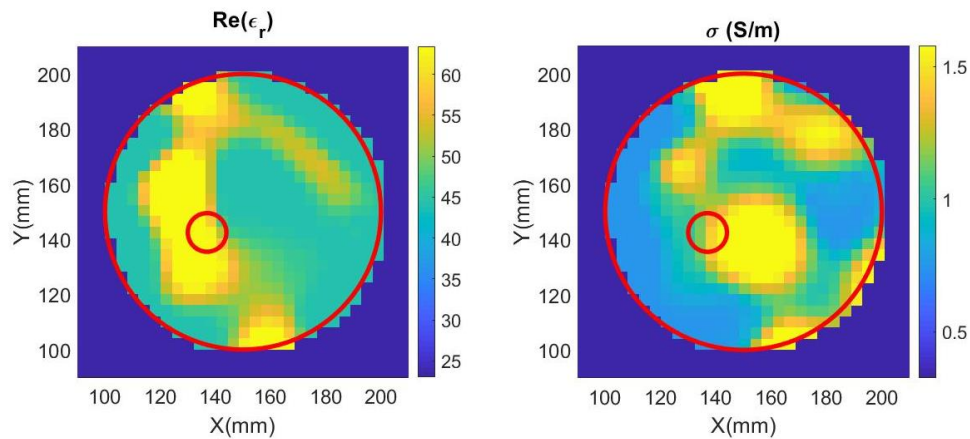


Figure 65: DBIM-TwIST reconstructions of electric properties without the contributions of neighbouring antennas. Input data: raw data with TG. On left  $\epsilon_r$  distribution, on right  $\sigma$  distribution.

Tissue	Expected	Results
Blood (1.0 GHz)	$\epsilon_r=63.41$ $\sigma=1.58$ S/m	$\epsilon_{r\_max}=84.51$ $\sigma_{max}=2.13$ S/m

Table 16: Comparison between expected and obtained electrical properties values.

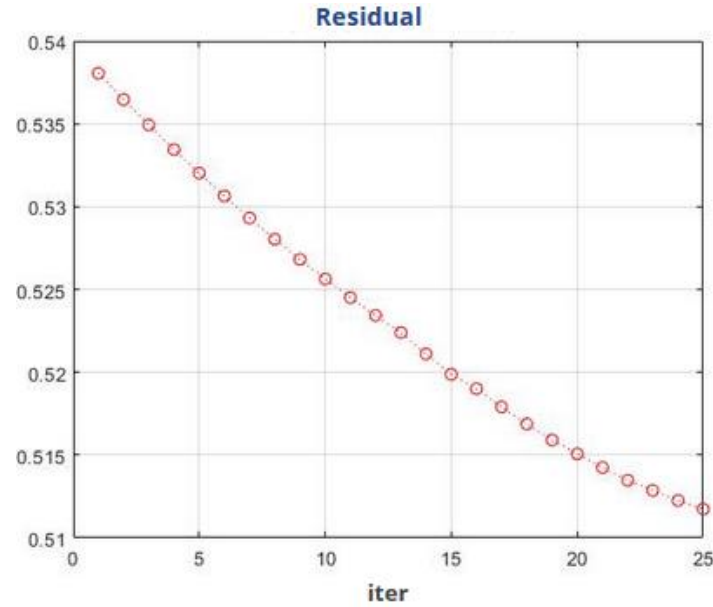


Figure 66: Residual at each iteration

- CS

Algorithm settings in the case raw data with TG, with TG without the contributions of neighbouring antennas and with calibration:

- Work frequency: 1.0 GHz
- Number of iterations: 15
- Tetrahedrons size: 2 mm

CS feels the presence of blood target but it has some problems with reconstructions: yellow pixels are located not only close to the right positions but they are sparse in almost whole the reconstruction domain.

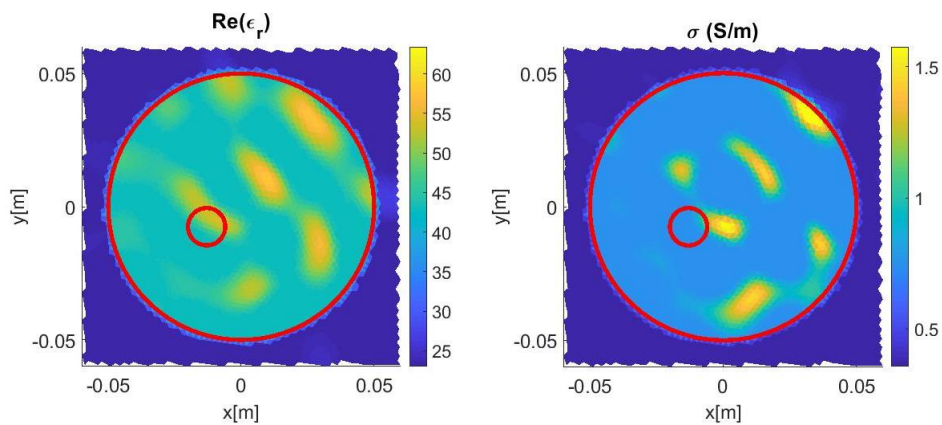


Figure 67: CS reconstructions of electric properties without the contributions of neighbouring antennas. Input data: raw data with TG. On left  $\epsilon_r$  distribution, on right  $\sigma$  distribution.

Moreover, it's difficult to find a number of iteration suitable because  $\epsilon_r$  is slower to reach the exact value, instead  $\sigma$  saturates very quickly (Table 17).

Tissue	Expected	Results
Blood (1.0 GHz)	$\epsilon_r=63.41$ $\sigma=1.58$ S/m	$\epsilon_{r\_max}=58.09$ $\sigma_{max}=1.92$ S/m

Table 17: Comparison between expected and obtained electrical properties values.

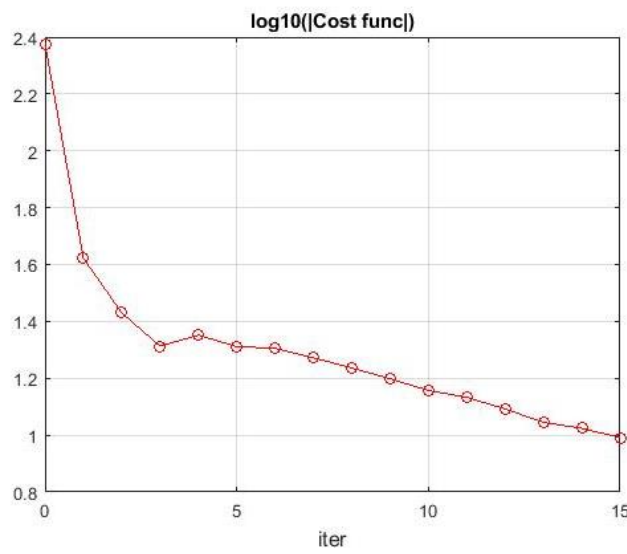


Figure 68: Cost functional at each iteration.

### 4.3.3 Case 3

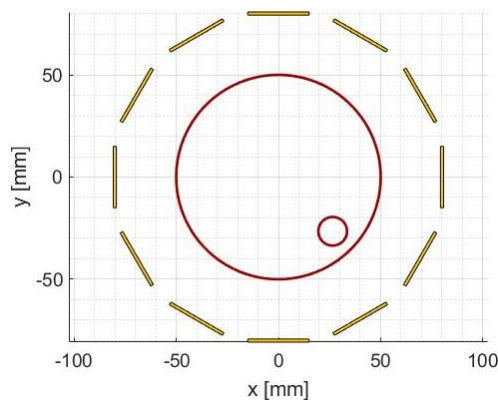


Figure 69: Geometry in case 3.

• *DBIM-TwIST*

Algorithm settings in the case raw data with TG, with TG without the contributions of neighbouring antennas and with calibration:

- Work frequency: 1.2 GHz
- Number of iterations: 25
- Resolution of the reconstructed image: 2 mm

As mentioned above, one step of the processing data is the contribution elimination of antennas close to the radiating one. The case 3 is the most difficult to reconstruct, because the target is very close to the antennas and the most important contribution is eliminated during processing.

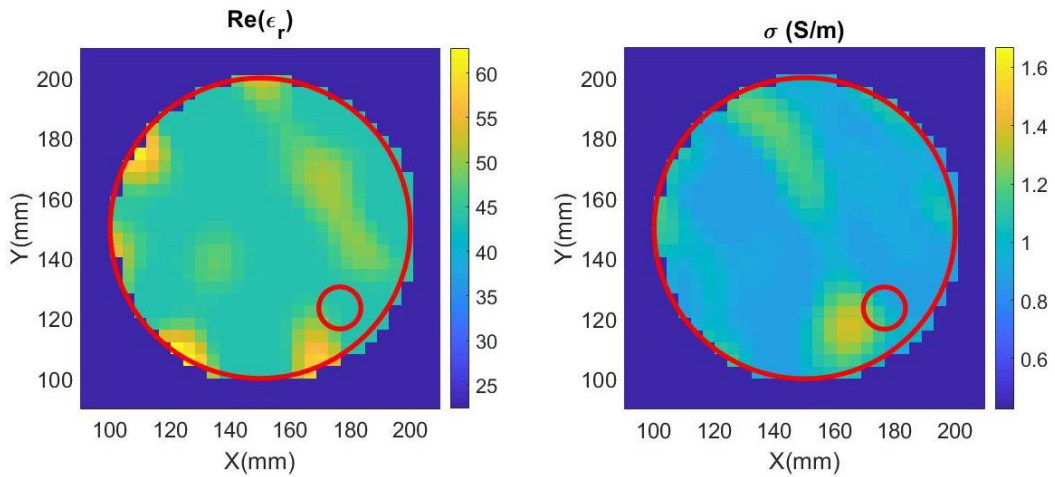


**Figure 70: DBIM-TwIST reconstructions of electric properties without the contributions of neighbouring antennas. Input data: raw data with TG. On left  $\epsilon_r$  distribution, on right  $\sigma$  distribution.**

In this case, the best results are obtained with 1.2 GHz as reported in Table 18.

Tissue	Expected	Results
Blood (1.2 GHz)	$\epsilon_r=62.81$ $\sigma=1.67$ S/m	$\epsilon_{r\_max}=66.54$ $\sigma_{max}=1.38$ S/m

**Table 18: Comparison between expected and obtained electrical properties values.**

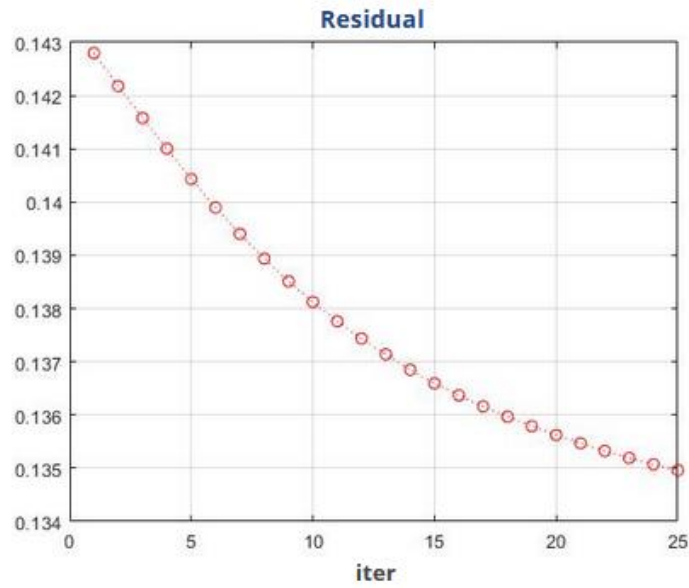


Figure 71: Residual at each iteration.

- CS

Algorithm settings in the case raw data with TG, with TG without the contributions of neighbouring antennas and with calibration:

- Work frequency: 1.0 GHz
- Number of iterations: 20
- Tetrahedrons size: 2 mm

The reconstructions in Figure 72 show the difficulty for CS to find the position and shape of blood target (as for the other models).

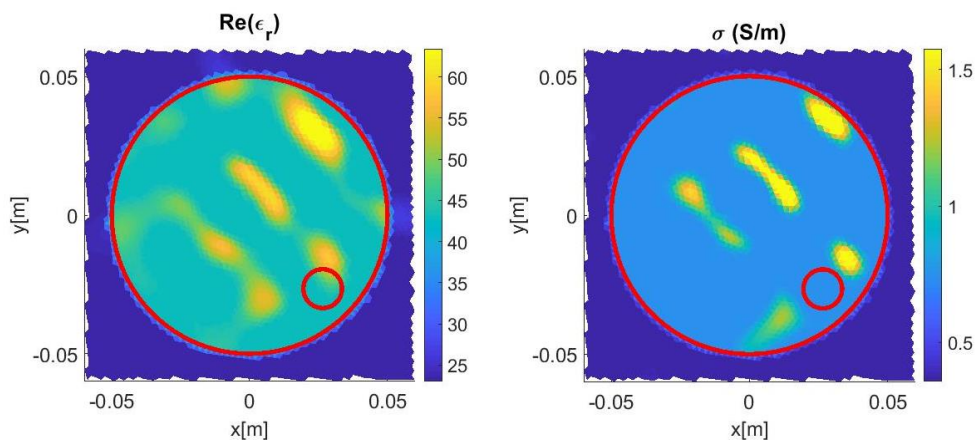


Figure 72: CS reconstructions of electric properties without the contributions of neighbouring antennas. Input data: raw data with TG. On left  $\epsilon_r$  distribution, on right  $\sigma$  distribution.

As for model 2, also in this case,  $\sigma$  saturates very quickly instead  $\epsilon_r$  is slower.

Tissue	Expected	Results
Blood (1.1 GHz)	$\epsilon_r=63.06$ $\sigma=1.62$ S/m	$\epsilon_{r,max}=71.02$ $\sigma_{max}=2.38$ S/m

Table 19: Comparison between expected and obtained electrical properties values.

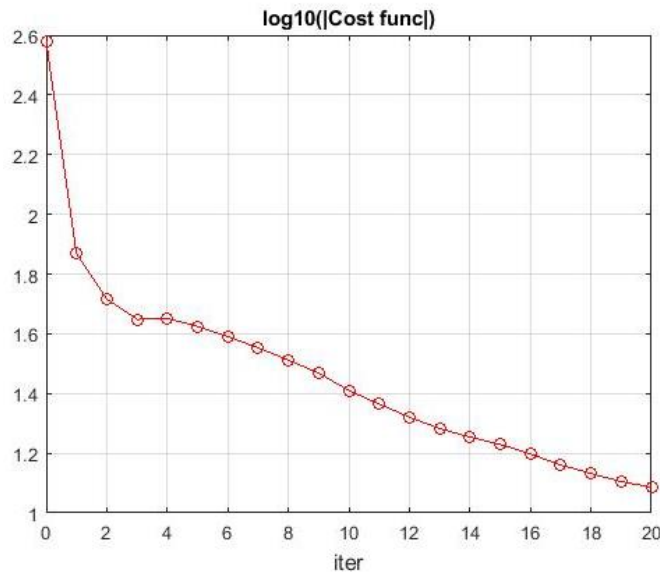


Figure 73: Cost functional at each iteration.

#### 4.3.4 SUMMARY

In conclusion, after all the tests performed on the different models, data processing steps are defined: Time Gating, Calibration with reference values and finally the contribute of neighbouring antennas has been eliminated.

The algorithms behave almost equally with the three models. DBIM results strictly depend from working frequency, but once you find the right frequency, the reconstructions can communicate some important information.

Instead, CS feels always the presence of the blood target but the reconstructions of it are always scattered in whole the domain.

# 5. CONCLUSIONS AND FUTURE DEVELOPMENTS

In this thesis, the overriding purpose is to analyze the performance of the DBIM and the CS in the case of interest: Microwave Imaging of post-stroke patients.

Algorithms validation is realized with known and trusted data, and the obtained results are consistent with what was expected for both the algorithms.

The next step is test with simulated data, in this case both the algorithms can recognize the presence of blood target and the domain region in which it's located. The DBIM has some problems with  $\varepsilon_r$  reconstruction, indeed it is able to trace only a halo around the right position. These results are due to the DBIM little flexibility to different type of discretization. Instead, the CS is able to find and reconstruct always the target in position and shape very close to the right ones, so it is more stable than the DBIM algorithm with different type of domain discretization.

In the last step, algorithms input are measured data. This is the most difficult case because of the presence of noise. Moreover, the algorithms approximations become more consistent and models used for calibration are really different from the real ones. DBIM performances strictly depend from working frequency, but when you find the correct frequency the results are significant. On the contrary, CS has a lot of difficulties in reconstructions: pixels with high values are distributed in almost whole the reconstruction domain.

Finally, according to the limitations of the current algorithms' performances, the future research could be developed from the following directions:

- Only for DBIM-TwIST, an important improvement is to make more stable and robust the domain discretization.
- As mentioned in chapter 2, both algorithms have different techniques to obtain convergence optimization. During this thesis, the algorithms have been used in their

basic form, to analyse the power of formulations, but one of the next steps could be performed on the optimized algorithms.

- A post processing of results could help to clean the reconstructed images, mostly in experimental testing.
- Geometries used to model the brain with stroke and the whole domain are really simple, a method to bring results closer to reality could be to create models with more details (external tank, more tissues in the brain and not only one tissue with properties equal to the average of all brain tissues, ...).
- Both the algorithms work in 2D, obviously this implies a lower computational cost, but also a lot of approximations. However, the goal is to reconstruct the entire volume of the head, therefore it's necessary to extend the algorithms to 3D.
- Finally, one of the most important problems for both the algorithms is the lack of an automatic stop mechanism. Therefore, the imposition of a threshold mechanism based on residual, allows to make the two algorithms completely automatic.

# BIBLIOGRAPHY

- [1] Wikipedia, "Stroke," [Online]. Available: [https://en.wikipedia.org/wiki/Stroke#Ischemic\\_2](https://en.wikipedia.org/wiki/Stroke#Ischemic_2). [Accessed 23 05 2019].
- [2] "BrainsGate, a new Path to Hope," [Online]. Available: [http://www.brainsgate.com/eng/page.php?id=3&instance\\_id=](http://www.brainsgate.com/eng/page.php?id=3&instance_id=). [Accessed 08 06 2019].
- [3] L. Jofre, *Microwave Medical Imaging - Antenna Imaging Techniques.*, Barcelona, 2015.
- [4] "Idaho Urologic Institute," [Online]. Available: <https://www.idurology.com/imaging-radiology/computed-tomography-ct>. [Accessed 23 09 2019].
- [5] M. I. Rosa Scapatucci, J. Tobon, G. Bellizzi, S. M. I. Francesca Vipiana and S. M. I. and Lorenzo Crocco, "Design and Numerical Characterization of a Low-Complexity Microwave Device for Brain Stroke Monitoring.," *IEEE*, vol. 66, no. 12.
- [6] "Risonanza Magnetica," [Online]. Available: <https://www.google.com/search?client=firefox-b-d&biw>. [Accessed 24 09 2019].
- [7] J. A. T. Vasquez, R. Scapatucci, G. Turvani, G. Bellizzi, N. Joachimowicz, B. Duchêne, E. Tedeschi, M. R. Casu, L. Crocco and F. Vipiana, "Design and Experimental Assessment of a 2-D Microwave Imaging System for Brain Stroke Monitoring," 02 2019.
- [8] J.-C. Bolomey and L. Jofre, "Three Decades of Active Microwave Imaging Achievements Difficulties and Future Challenges," *IEEE*, 2010.
- [9] N. Joachimowicz, B. Duchêne and C. C. a. O. Meyer, "Anthropomorphic Breast and Head Phantoms for Microwave Imaging," *MDPI*, 18 12 2018.
- [10] "Calculation of Dielectric Properties of Body tissues," 1997-2015. [Online]. Available: <http://niremf.ifac.cnr.it/tissprop/htmlclie/uniquery.php?func=atsffun&freq=>. [Accessed 15 07 2019].
- [11] S. M. I. Anthony E. Stancombe, M. I. Konstanty S. Bialkowski, A. M. Abbosh and

- I. Senior Member, “Portable Microwave Head Imaging System Using Software-Defined Radio and Switching Network,” 2018.
- [12] V. L. Coli, P.-H. Tournier, V. Dolean, I. E. Kanfoud, C. Pichot, I. M. Fellow and a. L. Blanc-Féraud, “Detection of Simulated Brain Strokes Using Microwave Tomography,” *APS/URSI*, no. 2454, 2018.
- [13] “Stroke Finder,” [Online]. Available: <https://www.chalmers.se/en/projects/Pages/Strokefinder.aspx>. [Accessed 23 07 2019].
- [14] [Online]. Available: <https://www.bbc.com/news/health-27866391>. [Accessed 25 09 2019].
- [15] “Microwave,” [Online]. Available: <https://en.wikipedia.org/wiki/Microwave>. [Accessed 13 05 2019].
- [16] R. Orta, *Lecture Notes on Trasmissons Line Theory*, Torino, 2017, pp. 105-106.
- [17] I. Sarwar, G. Turvani, M. R. Casu, J. A. Tobon, F. Vipiana, R. Scapatucci and a. L. Crocco, “Low-Cost Low\_Power Acceleration of a Microwave Imaging Algorithm for Brain Stroke Monitoring,” *MDPI*, 01 11 2018.
- [18] Z. Miao and S. M. I. and Panagiotis Kosmas, “Multiple-Frequency DBIM-TwIST Algorithm for Microwave Breast Imaging,” *IEEE*, vol. 65, no. 5, 05 2017.
- [19] Z. Miao and S. D. P. Kosmas, “Zhezhuang Miao, Supervisor: DImplementation and optimization of microwave medical imaging based on the multiple-frequency DBIM-TwIST,” 09 2017.
- [20] Z. Miao, S. Ahsan, P. Kosmas, J. T. Vasquez, F. Vipiana, M. Casu and M. Vacca, “Application of the DBIM-TwIST Algorithm to Experimental Microwave Imaging Data,” 11 2017.
- [21] G. Vecchi, *Electrodynamics of Continuum Media: Standard Media and Biological Tissues*, Torino, 2018.
- [22] “The Finite-Difference Time Domain Method,” [Online]. Available: <https://my.ece.utah.edu/~ece6340/LECTURES/lecture%2014/FDTD.pdf>. [Accessed 29 06 2019].
- [23] X. Xiao, X. Liu and B. Liu, “Study on Microwave Imaging for the Early Breast Cancer Detection by FDTD with PML Boundary Condition,” 2009.
- [24] P. M. v. d. Berg and a. A. Abubakar, “CONTRAST SOURCE INVERSION METHOD: STATE OF ART,” vol. Progress In Electromagnetics Research,

- 2001.
- [25] A. Abubakar, P. M. v. d. Berg and M. I. and Jordi J. Mallorqui, "Imaging of Biomedical Data Using Multiplicative Regularized Contrast Source Inversion Method," *IEEE*, vol. 50, no. 7, 07 2002.
- [26] P. M. v. d. Berg and a. R. E. Kleinman, "A contrast source inversion method," 1997.
- [27] P. M. v. d. Berg, A. L. v. Broekhoven and a. A. Abubakar, "Extended contrast source inversion," 1999.
- [28] A. Zakaria, C. Gilmore and a. J. LoVetri, "Finite-element contrast source inversion method for microwave imaging".
- [29] E. A. Attardo, F. I. Giuseppe Vecchi and S. M. I. and Lorenzo Crocco, "Contrast Source Extended Born Inversion in Noncanonical Scenarios Via FEM Modeling," *IEEE*, vol. 62, no. 9, 09 2014.
- [30] M. I. Amer Zakaria and S. M. I. and Joe LoVetri, "The Finite-Element Method Contrast Source Inversion Algorithm for 2D Transverse Electric Vectoria Problems," 2012.
- [31] C. Gilmore, P. Mojabi, A. Zakaria, M. Ostadrahimi, C. Kaye, S. Noghianian, L. Shafai, S. Pistorius and J. LoVetri, "A Wideband Microwave Tomography System With a Novel Frequency Selection Procedure," vol. 57, no. 4, 04 2010.
- [32] M. Asefi, I. Jeffrey, J. LoVetri, C. Gilmore, P. Card and J. Paliwal, "Grain bin monitoring via electromagnetic imaging," 2015.
- [33] "MiBraScan," [Online]. Available: <https://mibrascan.polito.it/index.php/consortium/>. [Accessed 23 09 2019].
- [34] K. Technologies, "Time Domain Analysis Using a Network Analyzer".
- [35] M. I. José M. Bioucas-Dias and S. M. I. Mário A. T. Figueiredo, "A New TwIST: Two-Step Iterative Shrinkage/Thresholding Algorithms for Image Restoration," *IEEE*, vol. 16, no. 12, 12 2007.
- [36] "Centro Medico Madonna delle Grazie," [Online]. Available: <httpswww.studioradiologiavinci.itservizi-radiologiaradiologia-tradizionale>. [Accessed 23 09 2019].